Med12 cooperates with multiple differentiation signals to facilitate efficient lineage transitions in embryonic stem cells

Max Fernkorn[1,2], Christian Schröter[1,2,*]

[1]Department of Systemic Cell Biology, Max Planck Institute of Molecular Physiology, 44227 Dortmund, Germany

[2]current address: Leiden Academic Centre for Drug Research, Leiden University, 2333 CC Leiden, The Netherlands

*Correspondence: c.schroter@lacdr.leidenuniv.nl

Abstract

Cell differentiation results from coordinated changes in gene transcription in response to combinations of signals. FGF, Wnt, and mTOR signals regulate the differentiation of pluripotent mammalian cells towards embryonic and extraembryonic lineages, but how these signals cooperate with general transcriptional regulators is not fully resolved. Here, we report a genome-wide CRISPR screen that reveals both signaling components and general transcriptional regulators for differentiation-associated gene expression in mESCs. Focusing on the Mediator subunit *Med12* as one of the strongest hits in the screen, we show that it regulates gene expression in parallel to FGF and mTOR signals. Loss of *Med12* is compatible with differentiation along both the embryonic epiblast and the extraembryonic primitive endoderm lineage, but impairs pluripotency gene expression and slows down transitions between pluripotency states. These findings suggest that *Med12* helps pluripotent cells to efficiently execute transcriptional changes during differentiation, thereby modulating the effects of a broad range of signals.

Introduction

Cell differentiation during development is regulated by a suite of extracellular signaling systems that trigger expression changes of large gene modules. To execute such complex transcriptional responses, the activity of intracellular signaling effectors must be integrated with that of general transcriptional regulators that direct the activity of RNA polymerase II. How the signaling systems associated with pluripotency and differentiation work together with general transcriptional regulators during early lineage transitions is still not fully resolved.

The earliest cell differentiation events of mammalian embryogenesis first segregate the extraembryonic trophoblast from the inner cell mass (ICM). In a second step, the ICM further differentiates into extraembryonic primitive endoderm (PrE) and the pluripotent embryonic epiblast (Epi), which ultimately forms the fetus (Chazaud & Yamanaka, 2016). Subsequently, epiblast cells transition from the naïve pluripotent state at pre-implantation to formative and then primed pluripotency as they prepare for germ layer differentiation (Kalkan & Smith, 2014; Nichols & Smith, 2009; Smith, 2017). Embryonic stem cells (ESCs) allow modeling both the differentiation towards an extraembryonic PrE identity, as well as transitions between different pluripotent states (Kalkan et al., 2017). Mouse ESCs (mESCs) can either be maintained in medium containing serum and the cytokine LIF, or in a ground state of pluripotency using serum-free N2B27 medium supplemented with LIF and two small molecule inhibitors that activate Wnt/beta-Catenin signaling and inhibit FGF/ERK signaling, respectively (2i + LIF; Ying et al., 2008). Efficient PrE differentiation from mESCs can be achieved from ground state pluripotency by the forced expression of GATA transcription factors together with active FGF/ERK signaling (Fujikura et al., 2002; Schröter et al., 2015; Wamaitha et al., 2015). Transitions between pluripotency states in contrast can be triggered by the removal of small molecule inhibitors from the culture medium alone (Kalkan et al., 2017; Neagu et al., 2020). Together with experiments in the mouse embryo, these stem cell models have provided a comprehensive picture of the signaling control of the early lineage transitions in the mammalian embryo. Both PrE differentiation and exit of epiblast cells from naïve towards formative and primed pluripotency require FGF/ERK signaling as well as Wnt signaling inhibition (Athanasouli et al., 2023; Chazaud & Yamanaka, 2016; Kang et al., 2013; Nichols et al., 2009). PrE differentiation further benefits from LIF signaling (Morgani & Brickman, 2015), whereas the progression of epiblast cells is promoted by the Notch signaling effector RBPJ (Kalkan et al., 2019), and the mTOR signaling effector TFE3 (Betschinger et al., 2013; Villegas et al., 2019).

Developmental signaling systems often culminate in the activation or deactivation of sequence-specific transcription factors. In eukaryotes, transmission of such transcription

61 factor activity changes into altered RNA polymerase activity at specific promoters requires
62 large multiprotein assemblies such as the Mediator complex that physically bridges between
63 transcription factors and the basal transcriptional machinery (Soutourina, 2018). The
64 mammalian Mediator complex is formed by up to 30 subunits. It can be subdivided into a head,
65 a core and a tail domain, and the transiently associated CDK8 module which consists of four
66 subunits: the CDK8 kinase, CCNC, MED12, and MED13 (Luyties & Taatjes, 2022; Soutourina,
67 2018). Unperturbed Mediator function is required for expression of most protein-coding genes
68 (Soutourina, 2018). Still, individual Mediator subunits have been linked to transcriptional
69 changes in response to specific signaling systems. Deletion of *Sur2,* which encodes the
70 MED23 subunit, for example abrogates transcriptional activation downstream of ERK-MAPK
71 signaling in mESCs (Stevens et al., 2002). The CDK8 module in particular has been implicated
72 in directing rapid changes in gene expression patterns in response to various stimuli, such as
73 serum stimulation (Donner et al., 2010; Luyties & Taatjes, 2022). Furthermore, CDK8 inhibition
74 in mouse and human ESCs impairs pluripotency exit, mirroring effects of MEK/ERK inhibition
75 (Lynch et al., 2020). MED12, which activates CDK8 function in the kinase module (Knuesel et
76 al., 2009; Park et al., 2018), is essential for axis elongation and the activation of Wnt target
77 genes during mouse development (Rocha et al., 2010). Together, these works suggest that
78 the transmission of specific developmental signals to RNA polymerase II activity can be
79 mapped to specific Mediator subunits. How general these mappings are or whether they are
80 context-dependent is however not clear. It is also not known how interference with Mediator
81 activity in pluripotent cells affects differentiation efficiency of different lineages.
82 Here, we aim at identifying factors that mediate transcriptional changes in response to
83 signaling events during early mammalian cell differentiation, using the expression of a
84 *Spry4*$^{H2B\text{-}Venus}$ reporter allele as read-out in a genome-wide CRISPR screen. This reporter is
85 an established indicator of developmental FGF/ERK signals, and its expression is switched
86 on in both Epi and PrE cells during preimplantation development (Morgani et al., 2018). Our
87 screen returns both known and new signaling inputs into *Spry4*$^{H2B\text{-}Venus}$ reporter expression,
88 as well as several components of the Mediator and Elongator complexes. Using epistasis
89 analysis, we demonstrate that *Med12*, one of the strongest hits in the screen, functions
90 independently of and in parallel to the FGF and mTOR signaling systems in pluripotent cells.
91 Functional assays showed that, while not strictly required for lineage transitions, loss of *Med12*
92 leads to impaired signal responsiveness during pluripotency transitions. Collectively, these
93 results point to new signal-independent functions of *Med12* that help cells to efficiently execute
94 lineage transitions in early development.

Results

A genome-wide CRISPR screen identifies signaling and transcriptional regulators of *Spry4* expression

The differentiation of pluripotent cells towards different lineages rests on transcriptional changes triggered by extracellular signals. To identify effectors of signal-regulated gene expression during cellular differentiation, we performed a genome-wide CRISPR screen using the expression of a Sprouty4 reporter as a read-out (Hanna & Doench, 2020; Morgani et al., 2018; Fig. 1A). We chose Sprouty4 because it is a known target gene of developmental FGF signals, and shows strong expression changes upon both Epi and PrE differentiation (Morgani et al., 2018; Fig. 1 Supp 1). In serum + LIF medium, the *Spry4* reporter is expressed due to paracrine FGF signals. We generated Cas9-expressing *Spry4*:H2B-Venus reporter cells and transduced them with the Brie gRNA library targeting protein-coding genes (Doench et al., 2016). To identify positive and negative regulators of *Spry4* reporter expression, we flow sorted cells with decreased and increased fluorescence at 6 and 9 days after transduction, and determined enriched guides in sorted fractions (Fig. 1A). We first analyzed perturbations leading to reduced reporter expression. Gene-targeting gRNAs were more strongly enriched in the sorted fractions compared to non-targeting controls (Fig. 1B, Fig. 1 Supp 2, Supp Table 1). We used the robust rank algorithm (RRA; W. Li et al., 2014) to combine information from multiple gRNAs and to rank genes in each of the four conditions (1% and 5% gate at both day 6 and day 9, Supp Table 1). This analysis revealed up to 17 individual genes with an FDR ≤ 0.05, and up to 26 genes with an FDR ≤ 0.2 (Fig. 1C, Fig. 1 Supp 2). We compiled a list of hits by selecting genes that were detected with an FDR of ≤ 0.05 in one condition, or with an FDR of ≤ 0.2 in at least two conditions (Fig. 1D). Protein-protein interaction network analysis with String-DB revealed that most of our hits fell into a small number of groups that were highly connected and associated with specific molecular functions (Szklarczyk et al., 2015; Fig. 1E). One of these groups contained the FGF signaling genes *Fgfr1, Grb2, Sos1,* and *Ptpn11*, as would be expected given the strong regulation of *Spry4* by FGF signaling. Another group contained several genes involved in protein glycosylation and specifically the synthesis of heparan sulfates, such as *Slc35b2*, *Ext1*, *Ext2*, and *Extl3*. Heparan sulfates are crucial co-factors for efficient FGF signaling (Ornitz & Itoh, 2015). Since pooled CRISPR screens detect mainly cell-autonomous functions of gene perturbations, the appearance of these hits indicates that surface-tethered heparan sulfates determine a cell's responsiveness to FGF signaling. Three further groups contained genes associated with ribosome biogenesis and translation (*Rpl9*, *Rpl18*, *Eif3i* and *Dhx37)*, as well as genes of the Elongator (*Elp2 – 6*, *Ikbkap*

129 and *Kti12*) and Mediator complexes (*Med10, Med12, Med16, Med24* and *Med25*, Fig. 1E),
130 raising the possibility that these factors could have gene- or signal-specific functions in
131 mESCs.
132 Next, to validate selected hits in an independent experimental setting, and to evaluate their
133 effect size, we knocked out individual candidate genes using the most enriched gRNA from
134 the screen. Since we were interested in mechanisms of transcriptional regulation, we focused
135 on hits related to the Mediator and Elongator complexes, but also included *Grb2* and *Ptpn11*
136 as a reference to evaluate the effects of perturbing FGF signal transduction, and *Sox2* and
137 *Fam98b* as candidates that could not clearly be linked to a functional group (Fig. 1E). Flow
138 cytometry showed that knockout of all tested candidates led to a reduction of mean
139 *Spry4*:H2B-Venus fluorescence levels, albeit to a different degree: Knockout of components
140 of the Elongator complex as well as *Fam98b* and *Sox2* affected Sprouty4:H2B-Venus
141 expression only mildly, whereas knockout of the FGF signaling genes *Grb2* and *Ptpn11* had
142 the strongest effect, although they did not reach the reduction achieved via pharmacological
143 inhibition of FGF signal transduction with the MEK inhibitor PD0325901 (PD03) (Fig. 1F, G).
144 Knockout of Mediator components reduced *Spry4*:H2B-Venus levels to different degrees, with
145 *Med12* having the strongest effect, reducing *Spry4*:H2B-Venus levels to 35.3% ± 1.6%
146 compared to control (Fig. 1F, G). Thus, our screen and validation establish *Med12* as a strong
147 candidate regulator of signal-dependent gene expression in mESCs.

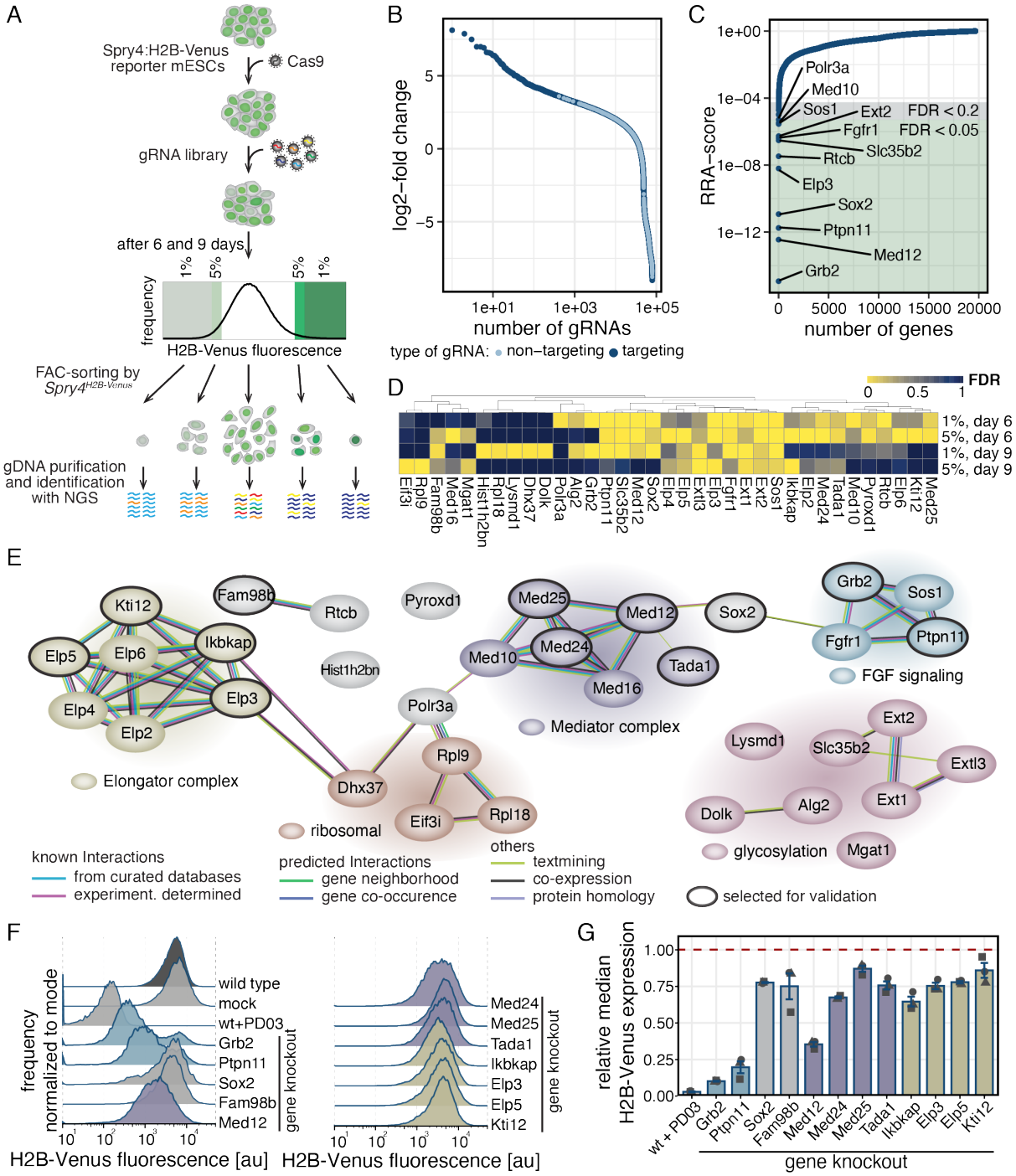

Fig. 1: Genome-wide CRISPR knockout screen reveals positive regulators of Sprouty4 expression.

A Schematic of the pooled CRISPR knockout screen. Cas9-expressing *Sprouty4*$^{H2B\text{-}Venus/+}$ reporter cells were transduced with a genome-wide gRNA library targeting protein-coding genes (Doench et al., 2016). Cells with in- or decreased fluorescence were flow sorted 6 or 9 days after transduction, and gRNAs enriched in sorted populations identified by sequencing.

B, **C** Enrichment of gene-targeting (dark blue) and control gRNAs (light blue) in cells sorted for the lowermost 1% of H2B-Venus signal 6 days after gRNA transduction, displayed as log2-fold change (B)

157 or RRA score of corresponding genes (C). Green and gray background in (C) indicates FDR < 0.05 and
158 < 0.2, respectively.
159 **D** Hierarchical clustering of gene perturbations leading to reduced *Spry4*$^{H2B\text{-}Venus}$ expression (FDR ≤
160 0.05 in at least one condition or FDR ≤ 0.2 in at least two conditions).
161 **E** Protein interaction network of genes shown in (D) based on String-DB. Background colors of genes
162 and gene clusters were manually assigned based on classification by functional similarity.
163 **F**, **G** H2B-Venus expression in *Spry4*$^{H2B\text{-}Venus/+}$ reporter cells upon knockout of selected candidate genes
164 6 d after transfection. (F) shows histograms of one representative experiment, (G) shows mean ± SEM
165 of median H2B-Venus expression from N = 3 independent experiments, normalized to fluorescence
166 levels in control wild-type cells (dashed red line). $p < 0.05$ for wild type vs. *Elp3*, *Elp5*, *Fam98b*, *Ikbkap*,
167 *Kti12*, *Med25* or *Tada1* knockouts; $p < 0.01$ for wild type vs. *Grb2*, *Med12*, *Med24*, *Ptpn11*, *Sox2*
168 knockouts or PD03-treated cells (Benjamin-Hochberg-adjusted, one-sided, paired t-test).
169
170 We next sought to use our screen to identify negative regulators of *Spry4* expression, by
171 looking at perturbations that led to increased reporter expression (Fig. 1A, right side of
172 histogram). Also here, gene-targeting gRNAs were enriched over control guides in the sorted
173 fractions (Fig. 2 Supp 1A-D, Supp Table 1). Ordering according to RRA-scores revealed up to
174 12 and 24 genes with FDR values of ≤ 0.05 and ≤ 0.2, respectively in each of the conditions
175 (Fig. 2A, Fig. 2 Supp 1E-G, Supp Table 1). Using the same criteria as for the positive
176 regulators, we compiled a list of 29 potential negative regulators of *Spry4* transcription (Fig.
177 2B). Analysis with String-DB again showed that many of these hits were highly connected and
178 associated with specific molecular functions (Fig. 2C). A large group of genes encoded
179 proteins that localized to mitochondria, or were otherwise associated with mitochondrial
180 functions. Several genes had signaling functions: *Lztr1* is a negative regulator of RAS-MAPK
181 and hence FGF signaling, in line with the strong representation of genes promoting FGF
182 signaling amongst the positive regulators of *Spry4* expression. We detected four genes that
183 were related to mTOR signaling (*Tsc1*, *Tsc2*, *Flcn*, and *Lamtor*). Finally, we found a big group
184 that contained genes involved in chromatin modification and transcription, amongst them three
185 genes encoding SWI/SNF related proteins. Thus, similarly to the collection of positive hits
186 identified above, our screen yields both signaling and transcriptional regulators that negatively
187 control *Spry4* expression. To select hits for validation, we focused on genes associated with
188 mTOR signaling, because these genes have also been implicated in the maintenance of
189 pluripotency (Betschinger et al., 2013; M. Li et al., 2018; Villegas et al., 2019). We also
190 included *Lztr1* as an FGF signaling gene, and *Smarcc1* as a representative of the group of
191 chromatin modifiers. Knockout of all six individual candidate genes with single gRNAs led to
192 an increase of mean *Spry4*:H2B-Venus fluorescence levels in reporter cells. The effect of
193 knocking out the mTOR signaling genes was stronger than that of knocking out *Lztr1* or

194 *Smarcc1*, and almost doubled reporter expression levels compared to mock-transfected cells
195 (Fig. 2D, E).

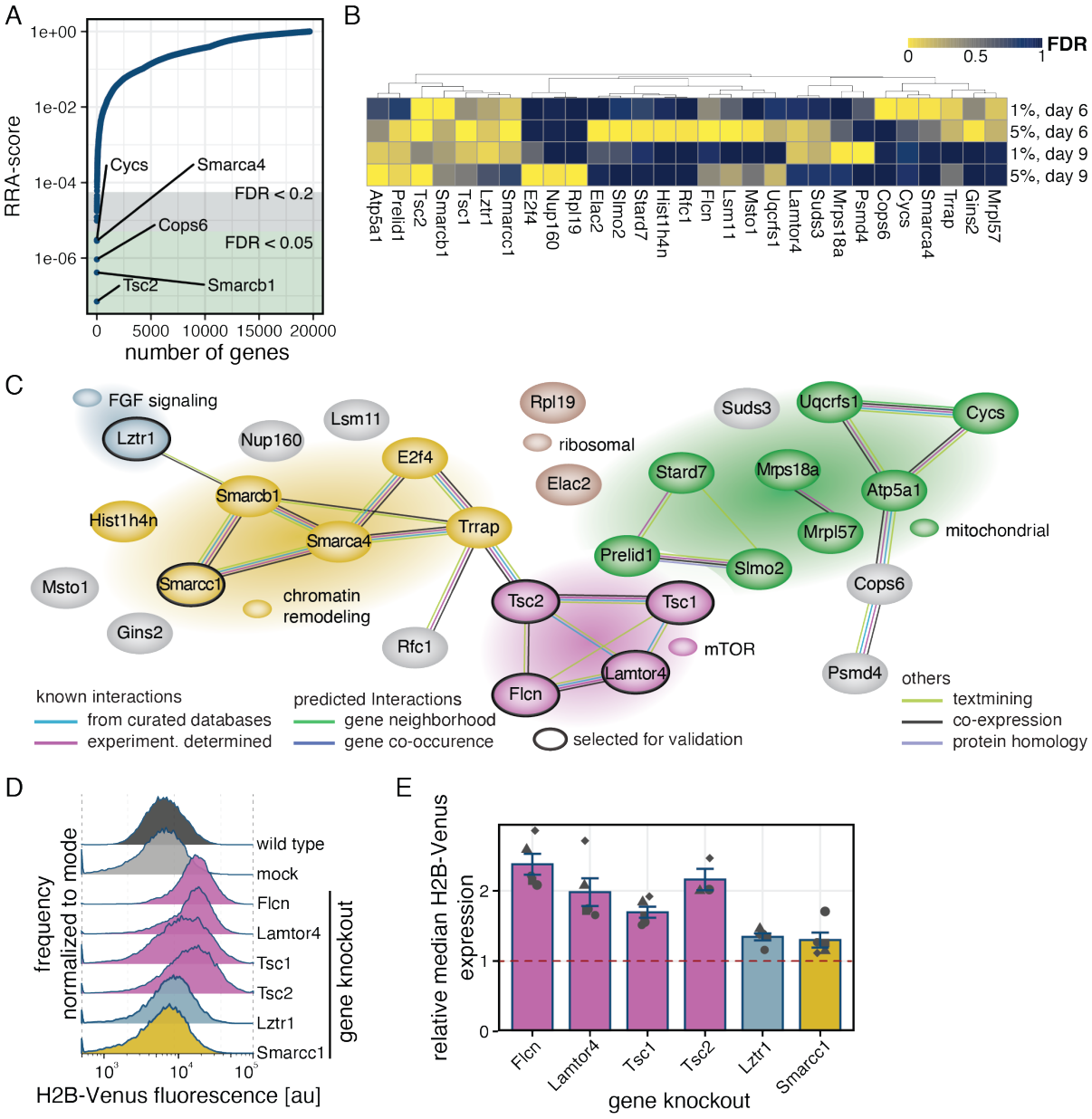

196
197 **Fig. 2: Genome-wide CRISPR knockout screen reveals negative regulators of Sprouty4**
198 **expression.**
199 **A** RRA scores of genes corresponding to gRNAs enriched in cells sorted for the topmost 1% of H2B-
200 Venus signal on day 6 after gRNA transduction.
201 **B** Hierarchical clustering of gene perturbations leading to increased *Spry4*$^{H2B\text{-}Venus}$ expression (FDR ≤
202 0.05 in at least one condition or FDR ≤ 0.2 in at least two conditions).
203 **C** Protein interaction network of genes shown in (B) based on String-DB. Background colors of genes
204 and gene clusters were manually assigned based on classification by functional similarity.
205 **D**, **E** H2B-Venus expression in *Spry*$^{H2B\text{-}Venus/+}$ reporter cells upon knockout of selected candidate genes
206 6 d after transfection. (D) shows histograms of one representative experiment, (E) shows mean ± SEM
207 of median H2B-Venus expression, N ≥ 3 independent experiments, normalized to fluorescence levels

208 in control cells transfected with a non-targeting control (dashed red line). $p < 0.05$ for mock-transfected
209 wild type vs. *Smarcc1* knockout; $p < 0.01$ for mock-transfected wild type vs. all other knockouts
210 (Benjamin-Hochberg-adjusted, one-sided, paired t-test).

211 *Med12* regulates gene expression in mESCs independently from 212 pluripotency-related signaling pathways

213 We then wanted to know how the signaling and transcriptional regulators identified in the
214 CRISPR-screen were functionally related. We focused on *Med12*, since of all transcriptional
215 regulators, it had the strongest effect on *Spry4* reporter expression. Furthermore, MED12 is a
216 component of Mediator's kinase module which could couple the activities of specific signaling
217 systems to transcriptional activity (Lynch et al., 2020; Rocha et al., 2010). To analyze *Med12*
218 functions in mESCs, we first generated monoclonal *Med12*-mutant cell lines. We generated
219 multiple independent clonal lines lacking part of exon 7, a region that was also targeted by
220 sgRNAs used in the CRISPR-screen, and confirmed the loss of MED12 protein expression by
221 immunoblotting (Fig. 3 Supp 1A, B). *Med12*-mutant cells grew normally in both serum + LIF
222 and 2i + LIF medium, and showed a reduced increase in *Spry4* reporter expression upon
223 switching from 2i + LIF to the N2B27 base medium (Fig. 3 Supp 1C, D). ppERK levels were
224 indistinguishable between wild-type and *Med12*-mutant lines (Fig. 3 Supp 1E, F), indicating
225 that reduced *Spry4* reporter expression is not due to deregulated FGF/ERK signaling.
226 Fluorescent in-situ hybridization revealed lower numbers of *Spry4* mRNAs in *Med12*-mutant
227 compared to wild-type cells Fig. 3 Supp 1G, H), suggesting that *Med12* regulates reporter
228 expression transcriptionally. Intriguingly, we also found slightly lower numbers of *Nanog*
229 mRNAs in *Med12* mutants in 2i medium, indicating that *Med12* could be quantitatively involved
230 pluripotency gene expression.
231 To assess gene expression differences between wild-type and *Med12*-mutant cells more
232 globally, we therefore performed bulk RNA sequencing of cells in 2i medium and upon 24 h of
233 differentiation in N2B27 (Fig. 3A). Principal component analysis separated samples in
234 pluripotency and differentiation medium along PC1 (32.1% of variance), and wild-type and
235 *Med12*-mutant cells along PC2 (16.8% of variance, Fig. 3B). Fewer genes were differentially
236 expressed between pluripotency conditions and 24 h in N2B27 in *Med12*-mutant compared to
237 wild-type cells. Most genes that were differentially expressed in the mutant were also
238 differentially expressed in the wild type (Fig. 3C, left, Supp Table 2). When comparing between
239 wild-type and *Med12*-mutant cells within each culture condition, we found that more genes
240 were differentially expressed between the two genotypes in N2B27 than in 2i (Fig. 3C, right,
241 Supp Table 2). Thus, loss of *Med12* impairs gene expression changes at the exit from
242 pluripotency. *Med12* has a closely related paralogue named *Med12l*. *Med12l* expression was

243 upregulated in *Med12*-mutant cells (Fig. 3 Supp 2A), and *Spry4* reporter expression in *Med12*-
244 mutant lines could be further reduced by simultaneously knocking-out *Med12l* (Fig. 3 Supp
245 2B). Thus, it is possible that *Med12l* partially compensates for loss of *Med12* function in the
246 mutant lines.
247 Exit from pluripotency is regulated by the interplay of a set of signaling systems, such as
248 mTOR, Notch, Wnt, and FGF (Betschinger et al., 2013; Kalkan et al., 2019; Ying et al., 2008).
249 We next asked if gene expression downstream of any of these signaling systems was affected
250 by loss of *Med12*, using previously defined sets of target genes specific for each signaling
251 system (Lackner et al., 2021). A strong expression change of such a set of target genes
252 between wild type and mutant cells can be considered a footprint of the perturbation of the
253 corresponding signaling system. We quantified this footprint of the loss of MED12 by
254 comparing the gene expression changes of the defined list of target genes during 24h of
255 differentiation between the wild-type and the mutant. This gene expression footprint was
256 strongest for mTOR target genes, less pronounced for Notch and Wnt target genes, and
257 virtually absent for FGF target genes (Fig. 3D, top row). In comparison to previously described
258 examples (Fig. 3D, lower rows, Lackner et al., 2021)) for signal-specific perturbations, the
259 effects of the loss-of MED12 appeared less specific for a single pathway. We functionally
260 tested the relationship between *Med12* and mTOR signaling by knocking out the mTOR
261 signaling genes *Flcn*, *Lamtor4*, *Tsc1* and *Tsc2* in *Med12*-mutant *Spry4*$^{H2B\text{-}Venus/+}$ cells. Similarly
262 to the situation in the wild type, knockout of these genes led to increased reporter expression,
263 albeit from a lower baseline level (Fig. 3E). Therefore, *Med12* regulates *Spry4* expression
264 independently from mTOR signaling. In addition to mTOR signaling genes and Mediator
265 subunits, our CRISPR screen revealed a large number of genes involved in FGF signal
266 transduction, but the footprinting analysis suggested that FGF inputs into gene expression
267 were independent from *Med12*. To further corroborate this result, we generated *Med12*
268 mutations in the background of an *Fgf4*-mutant mESC line, which allowed us to specifically
269 analyze the effects of FGF signaling upon the switch from pluripotency to differentiation
270 medium. We wanted to focus on immediate gene expression changes triggered by FGF
271 signaling, and therefore analyzed gene expression changes by bulk RNA-sequencing after 6
272 h of transfer into N2B27 medium with or without addition of exogenous FGF (Fig. 3F). Again,
273 principal component analysis showed that cells in pluripotency and differentiation medium
274 were separated along PC1 (33.2% of variance), and wild-type and *Med12*-mutant cells
275 separated along PC3 (9.3% of variance), both when analyzing independent *Med12*-mutant
276 clonal cell lines as well as experimental replicates (Fig. 3G). If expression of FGF target genes
277 was generally dependent on *Med12,* we would expect that their fold-change is lower in *Med12*-
278 mutant compared to wild-type cells, and that the number of differentially expressed genes
279 would be higher in the wild-type than in the *Med12*-mutant. However, when plotting the fold

280 expression-change for each gene upon 6 h of FGF stimulation for wild-type versus *Med12*-
281 mutant cells, we found that the majority of genes were induced to a similar degree in both
282 genotypes (2006 genes), while similar numbers of only 926 and 935 genes were differentially
283 expressed in the wild-type or the *Med12*-mutant only (Fig. 3H, Supp Table 3). Furthermore,
284 the ratios of fold-change values of FGF target genes between *Med12*-mutant and wild-type
285 cells showed a unimodal distribution with a mode of 1.068 for downregulated and 0.927 for
286 upregulated genes (Fig. 3J). While this slight deviation of the mode from 1 leaves open the
287 possibility that *Med12* influences their expression magnitude, overall these results argue
288 against a strong and specific role of *Med12* in the regulation of FGF target genes.
289

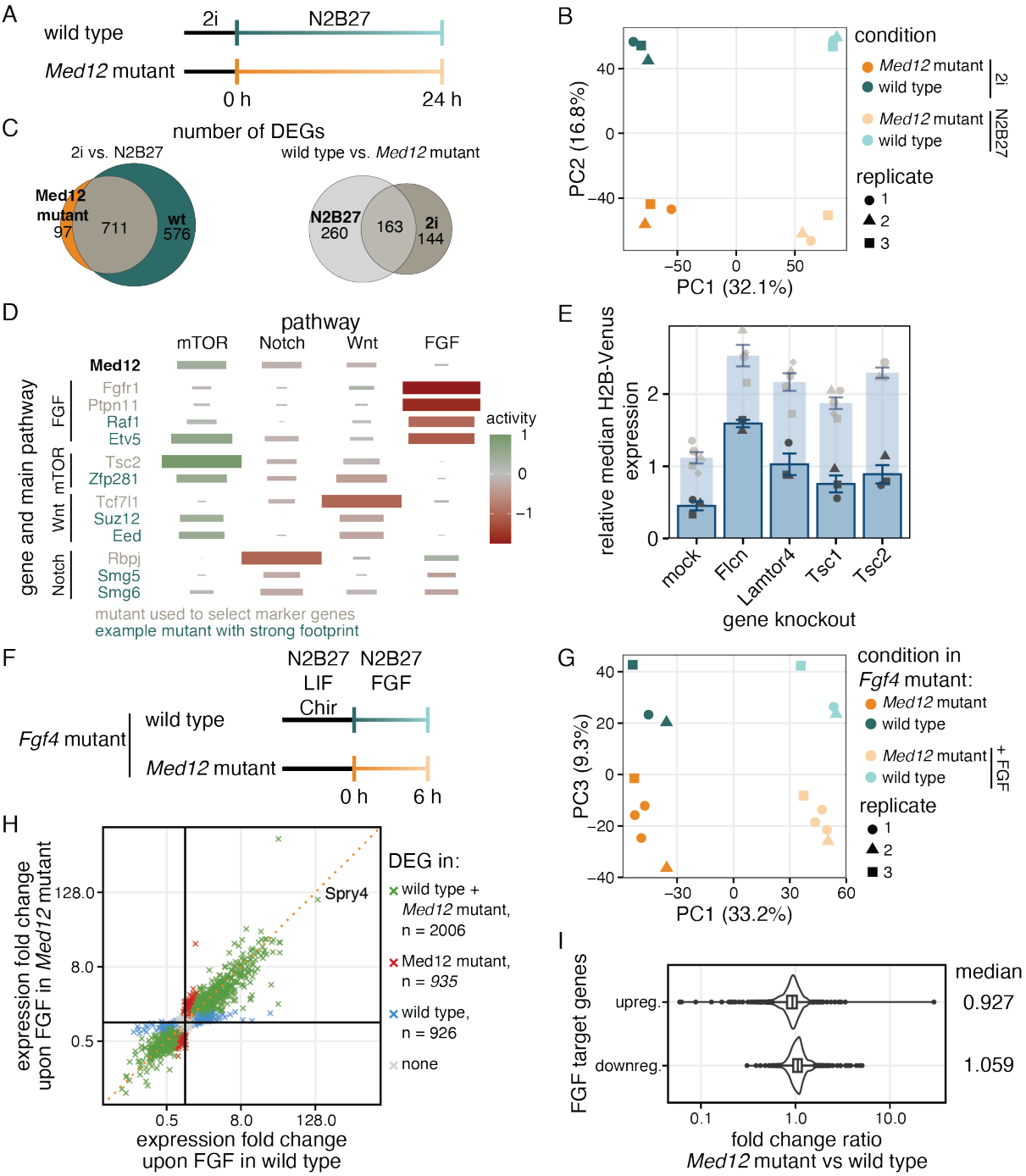

Fig. 3: *Med12* affects gene expression independently of pluripotency related signaling systems.

A Schematic of experiment to identify *Med12*-regulated genes by bulk RNA sequencing.

B Principal component analysis transcriptomes from (A).

C Euler-diagram showing the number differentially expressed genes (log2-fold change > |1|, adjusted p-value < 0.01) in bulk transcriptomes. Left panel compares genes differentially expressed upon 24 h of differentiation between *Med12*-mutant and wild-type cells, right panel compares genes differentially expressed upon loss of *Med12* between N2B27 and 2i.

D Expression footprint analysis using a set of 50 marker genes per pathway defined in (Lackner et al., 2021). Top row shows footprint of *Med12*-mutant cells. Lower rows show expression footprints of mutants from Lackner et al., 2021, for comparison. Gray: Mutants that were used to select marker

genes. Green: Independent example mutants that show a strong and specific footprint of one of the pathways. Tile color indicates relative pathway activity, tile size indicates spearman correlation of the expression of footprint genes with pathway-defining mutants (Lackner et al., 2021).

E Median H2B-Venus fluorescence upon mutation of mTOR related genes in *Med12*-mutant *Spry4*$^{H2B\text{-}Venus/+}$ cells, normalized to H2B-Venus expression in *Med12* wild-type cells. Median H2B-Venus fluorescence upon mutation of mTOR related genes in *Med12* wild-type cells is reproduced from Fig. 2E for comparison (light blue). Error-bars indicate SEM, points individual replicates, N ≥ 3 independent experiments.

F Schematic of experiment to test *Med12*-dependency of FGF target genes by RNA sequencing.

G Principal component analysis transcriptomes from (F). PC2 (not shown; 12.8% of variance) separated experimental replicates from each other.

H Gene expression fold changes and number of significantly differentially expressed genes (adjusted p-value < 0.01) upon FGF4 stimulation in wild-type versus *Med12*-mutant cells. Dotted orange line indicates the unity line.

I Ratio of expression fold changes for FGF target genes between wild-type and *Med12*-mutant cells, for up- (top) and downregulated genes (bottom). FGF target genes were defined as having a log2-fold change in wild-type cells upon FGF4 stimulation > |1| and an adjusted p-value < 0.05.

Extraembryonic endoderm differentiation in *Med12* mutant cells

Loss of the Mediator subunit Med24 compromises PrE differentiation (Hamilton et al., 2019). We therefore asked if *Med12* was likewise required for the segregation of Epi and PrE identities, using their differentiation of upon transient expression of GATA6-mCherry as a model system (Fig. 4A, Schröter et al., 2015). A mix of SOX17-positive PrE cells and NANOG-positive Epi cells differentiated irrespective of *Med12* status, but the fraction of PrE cells was lower, and that of Epi cells was higher in mutant compared to wild-type cultures (Fig. 4B, C). Those differences in cell type ratios could not be rescued by supplementing the differentiation medium with FGF4 (Fig. 4 Supp. 1A, B). However, similarly high proportions of PrE cells differentiated from both wild-type and *Med12* mutant cells when cells sorted for high GATA6-mCherry levels were treated with FGF4 during differentiation (Fig. 4 Supp. 1C, D), indicating that the main cause for these ratio differences were lowered expression levels of the GATA6-mCherry transgenes in *Med12* mutant cell lines compared to wild type (Fig. 4D). This conclusion was further corroborated when we connected GATA6-mCherry expression levels with differentiation outcome in individual cells through live-cell imaging followed by immunostaining for fate markers (Schröter et al., 2015). GATA6-mCherry levels rose more slowly and reached lower peak levels in the mutant relative to wild type, even when using longer induction times (Fig. 4 Supp 1F). Still, PrE differentiation could be predicted based on GATA6-mCherry expression levels with similar precision in both wild-type and *Med12* mutant

338 cells (Fig. 4 Supp. 1 G – I), and GATA6-mCherry threshold values required to trigger PrE
339 differentiation appeared even slightly lowered in *Med12* mutant cells (Fig. 4 Supp. 1 J). Thus,
340 loss of *Med12* impairs transgene induction levels but not general PrE differentiation potential.
341 To test if loss of *Med12* had more subtle effects on PrE differentiation, we performed single-
342 cell RNA sequencing (scRNAseq) of wild-type and *Med12*-mutant cells in pluripotency
343 conditions, and after GATA6-mCherry induction for 4 h (wild type) or 8 h (*Med12* mutants)
344 followed by 20 h of differentiation (Fig. 4E). Cells from 2i + LIF (pluripotency) and N2B27
345 medium (differentiation) formed two distinct groups in UMAP space that were marked by
346 expression of the Wnt/β-Catenin target Sp5 (pluripotency) or differentiation marker Dnmt3l,
347 respectively (differentiation) (Fig. 4F, G). Within both the pluripotency and the differentiation
348 group, wild type and *Med12*-mutant cells segregated from each other, indicating that loss of
349 *Med12* affected single-cell transcriptional state in both conditions (Fig. 4F). In the
350 differentiation group, the PrE markers Sox17, Dab2, and Cubn and the Epi markers Nanog
351 and Fgf4 showed a mutually exclusive expression pattern in both wild-type and *Med12*-mutant
352 cells (Fig. 4G), providing an opportunity to compare lineage-specific effects of the loss of
353 *Med12* between Epi and PrE cells. To consistently identify Epi and PrE cells across genotypes,
354 we integrated the five differentiated samples and clustered them to separate two major groups
355 that were separated along in principle component space (Fig. 4H). *Gata6* and *Nanog*
356 expression identified these two clusters as PrE (cluster 0) and Epi (cluster 1), respectively
357 (Fig. 4H, I, Supp Table 4). The proportion of PrE cells in this dataset was again lower in *Med12*
358 mutants compared to wild-type, consistent with immunostaining results (Fig. 4J). To evaluate
359 the roles of *Med12* on lineage-specific gene expression changes upon differentiation, we first
360 selected genes that had a log2 fold change $\geq$ 0.5 between pluripotency and differentiation in
361 wild-type cells and plotted their fold-change in the mutant (Fig. 4K). These fold-changes
362 showed a unimodal distribution in all four conditions (up- and downregulation, Epi and PrE
363 differentiation). Furthermore, when plotting the fold-change of all genes upon differentiation
364 against each other for wild-type and mutant cells, we found that data points uniformly clustered
365 around the line of unity (Fig. 4 Supp 3 A, B). Finally, many of the top differentially expressed
366 genes between wild type and mutant were the same in all in pluripotent, Epi, and PrE cells
367 (Fig. 4 Supp 3 A, B, Supp Table 5). Taken together, these results suggest that loss of *Med12*
368 does not affect specific gene modules during differentiation. but rather results in gene
369 expression changes that are shared between differentiated states.
370 Prompted by the observation that GATA6-mCherry induction levels were consistently lowered
371 in *Med12* mutant cells, we asked if loss of *Med12* had more global effects on transcriptional
372 output and mRNA levels in cells. The multiplexed nature of our dataset allowed us to compare
373 mRNA levels between conditions, revealing that differentiation led to an increase in captured

374 mRNAs in both wild-type and mutant cells (Fig. 4 Supp. 3A). Furthermore, less mRNAs were
375 captured from differentiated *Med12* compared to wild type cells (median number of UMIs
376 28227 and 25649, respectively, Fig. 4 Supp 3 A). While EU-labelling of newly synthesized
377 RNAs suggested that higher mRNA content in differentiated compared to pluripotent cells
378 were associated with increased transcriptional output, we could not detect significant
379 differences in EU-labelling between wild-type and *Med12* mutant cells (Fig. 4 Supp 3 B – E).
380 This leaves open the possibility that reduced mRNA levels in *Med12* mutant cells arise from
381 effects other than reduced transcriptional output.

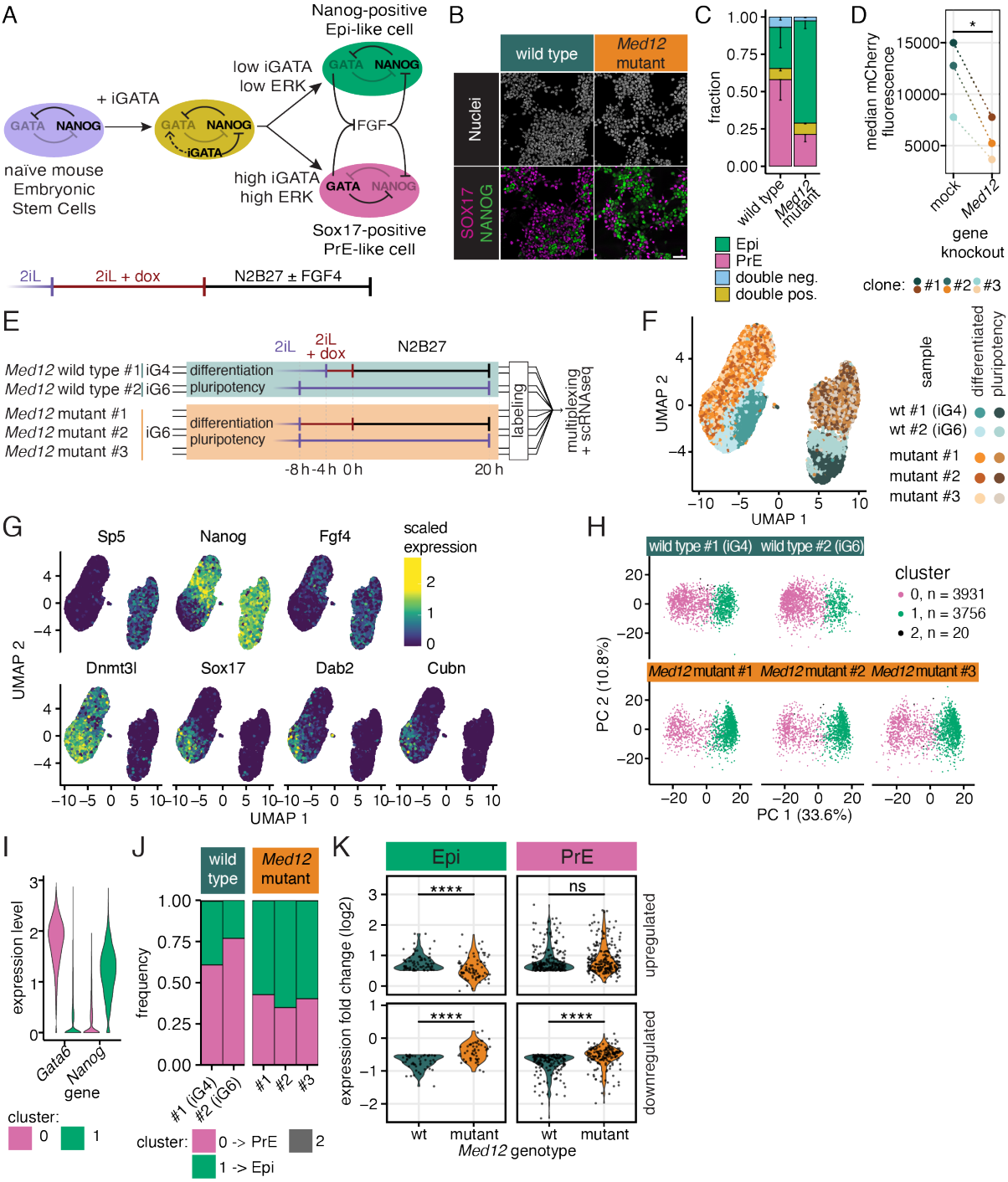

382
383

384 **Fig. 4: Role of *Med12* in PrE differentiation.**
385 **A** Schematic of experimental approach to model differentiation of mESCs towards epiblast and primitive
386 endoderm via GATA induction.
387 **B** Immunostaining for the Epi-marker NANOG (green) and the PrE marker SOX17 (magenta) after 8 h
388 of GATA6 induction followed by 20 h of differentiation in wild-type and *Med12*-mutant cells. Scale bar:
389 50 µm.
390 **C** Cell type proportions in wild-type and *Med12*-mutant cells differentiated as in (B). N = 3, n > 1100
391 cells per replicate, error bars indicate SEM.
392 **D** Median Gata6-mCherry fluorescence upon 8h dox induction in three independent clonal GATA6-
393 mCherry inducible cell lines 7 days after transfection with control or *Med12*-targeting gRNAs. * indicates
394 $p \leq 0.05$, paired student's t-test.
395 **E** Schematic of the single cell RNA sequencing experiment to compare single cell transcriptional
396 signatures between wild-type and *Med12*-mutant cells in pluripotency and upon PrE differentiation. Two
397 *Med12* wild-type lines carrying inducible GATA4- or GATA6-mCherry transgenes (iG4 and iG6), and
398 three independent *Med12*-mutant cell lines derived from the GATA6-mCherry inducible line were
399 included as replicates. Samples were multiplexed and pooled before mRNA capture and library
400 preparation to minimize batch effects. Doxycycline induction was 4 h and 8 h in wild-type and *Med12*-
401 mutant cells, respectively.
402 **F** UMAP plot of single cell transcriptomes from all 10 samples.
403 **G** Ln-scaled expression levels of selected marker genes projected onto the UMAP plot from (F).
404 **H** Principal component analysis and Louvain-clustering of single-cell transcriptomes from wild-type and
405 *Med12*-mutant cells after differentiation.
406 **I** Ln-transformed expression levels of the PrE-marker gene *Gata6* and the Epi-marker gene *Nanog* in
407 the differentiated samples split by cluster. Cluster 2 was excluded due to the small number of cells.
408 **J** Proportions of cell types in the sequencing experiment, identified by clustering, in wild-type and
409 *Med12*-mutant cells.
410 **K** Comparison of up- (top panels) and downregulated genes (bottom panels) in wild-type and *Med12*-
411 mutant cells upon differentiation from pluripotency to Epi (left) or PrE (right). Shown are genes with a
412 log2-change of expression > 0.5 in wild-type cells. ns indicates $p \geq 0.05$, **** indicates $p \leq 0.0001$,
413 paired Wilcoxon signed rank test.
414 For clarity, measurements from the two *Med12* wild-type and the three *Med12*-mutant lines were pooled
415 in panels I and K.
416

417 *Med12* regulates dynamics of pluripotency transitions

418 Besides bridging between signals, sequence-specific transcription factors and the core
419 transcriptional machinery, the Mediator complex also regulates enhancer-promoter
420 interactions in ESCs (Kagey et al., 2010). We reasoned that impaired reconfiguration of these
421 contacts might impact differentiation dynamics, and therefore tested how pluripotency
422 transitions were affected by loss of *Med12.* We first probed exit from naïve pluripotency with

423 a colony formation assay (Kalkan et al., 2017), where we differentiated cells in N2B27 for 48
424 h, followed by seeding at clonal density in 2i + LIF medium (Fig. 5A). Because we grew cells
425 in the presence of LIF before transfer into N2B27, wild-type cells still formed a large number
426 of pluripotent colonies (Lackner et al., 2021). In *Med12*-mutant cells in contrast, the number
427 of pluripotent colonies was significantly reduced (Fig. 5B, left, Fig. 5 Supp 1A, Supp Table 6).
428 To test how stable this phenotype is under different signaling conditions, we carried out the
429 same colony assay in an *Fgf4* mutant background. Upon supplementation of N2B27 with
430 FGF4, the number of pluripotent colonies formed by *Fgf4; Med12* double mutant cells was
431 much reduced, both compared to the *Fgf4* single mutant supplemented with FGF4, and the
432 *Fgf4; Med12* double mutant in the absence of FGF4 (Fig. 5B, right, Fig. 5 Supp 1B). Although
433 we cannot rule out the possibility that the use of FBS required for the proliferation of *Fgf4*
434 mutant cells in 2i + LIF medium (Raina et al., 2021) had selective effects on the *Med12* mutant
435 cells, these results suggest that loss of *Med12* impairs the ability of single cells to re-establish
436 a gene expression profile compatible with growth in 2i + LIF following transient differentiation
437 in N2B27.
438 The ability to form pluripotent colonies in the colony formation assay depends on a cell's
439 pluripotency state at the beginning of the differentiation period, and its ability to react to
440 changing culture conditions. We used our bulk RNA sequencing data comparing wild-type and
441 *Med12*-mutant cells after 24 h in N2B27 to evaluate which of these properties were affected
442 upon loss of *Med12*. We first determined differentiation delays of the two genotypes using a
443 published high time-resolution reference dataset (Lackner et al., 2021). Surprisingly, this
444 analysis indicated that *Med12*-mutant cells differentiated more slowly than the wild-type (Fig.
445 5C). This could be a consequence of stronger expression of naïve genes in pluripotency
446 conditions, or reflect slower downregulation of these genes in N2B27 in the *Med12* mutant. To
447 distinguish between these possibilities, we plotted the expression levels of 7 selected
448 pluripotency marker genes in 2i and after 24 h in N2B27 in wild-type versus *Med12*-mutant
449 cells. In this plot, data points above and below the unit line indicate higher and lower
450 expression in the mutant relative to the wild type, respectively, and the slope of the connecting
451 line between expression in 2i and N2B27 indicates the dynamics of down-regulation (Fig. 5D,
452 left). We found that in 2i medium, all marker genes were less strongly expressed in the mutant
453 compared to the wild type. Consistent with our results from bulk RNA sequencing, expression
454 levels of the pluripotency genes in the single-cell RNA sequencing dataset (Fig. 4E) *Klf4*,
455 *Zfp42*, and *Tbx3* were reduced in the mutant cells, whereas levels of *Prdm14*, *Nanog*, *Esrrb*,
456 and *Tcf21l1* were similar between the two genotypes (Fig. 5 Supp 1C). Furthermore, their
457 slopes during differentiation were consistently smaller than one (Fig. 5D). Such a systematic
458 reduction in the slope of downregulation was also observed when we analyzed the top 100
459 downregulated genes in wild-type or *Med12*-mutant cells (Fig. 5E, left). Upregulation of genes

is similarly affected, as the top 100 upregulated genes also showed a slope lower than 1 (Fig. 5E, right). Since a loss of Oct4 (POU5F1) can be sufficient to block the differentiation potential of mESCs (Radzisheuskaya et al., 2013), we checked the protein expression level by immunostaining (Figure 5 Supp 1C). However, there was no significant difference in expression levels between *Med12*-mutant and wild-type cells (Figure 5 Supp 1D). Taken together, these results indicate that *Med12* mutant cells show an impaired pluripotency gene expression profile as well as a slowed reconfiguration of gene expression programs upon changing culture conditions, thereby implicating *Med12* as a global regulator of pluripotency transition dynamics.

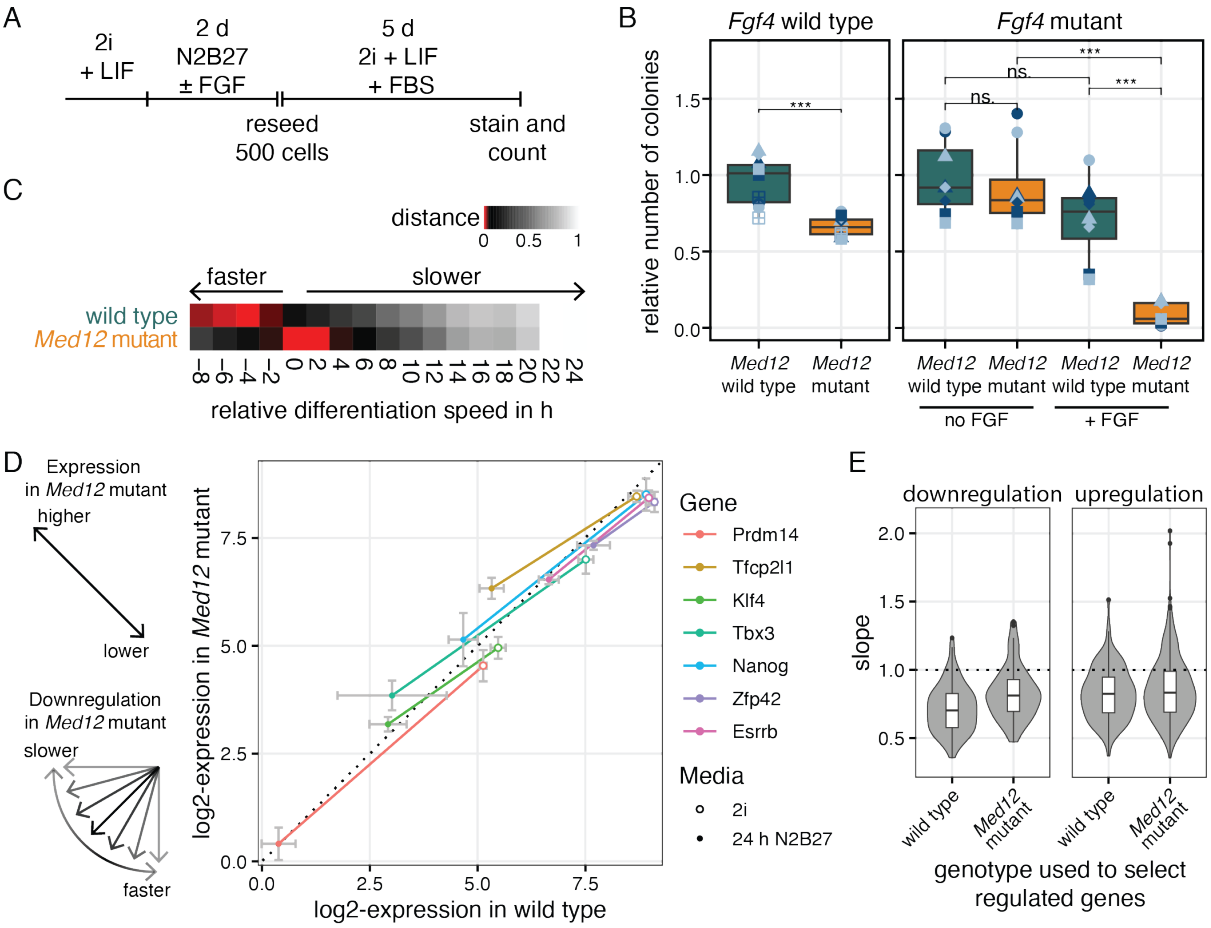

Fig. 5: Mutation of *Med12* affects dynamics of pluripotency transitions.

A Experimental approach to determine clonogenicity of *Med12*-mutant and wild-type cells. 2i + LIF was supplemented with FBS to support growth of *Fgf4*-mutant cells after reseeding.

B Number of colonies after treatment as indicated in (A) for both wild-type and *Med12*-mutant cells in an *Fgf4* wild-type (left) and *Fgf4* mutant background with and without supplementation with 10 ng/µL FGF4 (right). N ≥ 4 independent experiments, same symbols in different colors indicate technical replicates within an independent experiment. ns indicates $p \geq 0.05$, *** indicates $p \leq 0.001$, paired Wilcoxon signed rank test.

C Estimation of differentiation delay in wild-type and *Med12*-mutant cells, relative to a published time resolved gene expression dataset (Lackner et al., 2021). Plot shows the normalized Euclidean distance

480 of the expression of naïve marker gene panel (*Prdm14*, *Tfcp2l1*, *Klf4*, *Tbx3*, *Nanog*, *Zfp42*, *Esrrb*) to
481 the reference dataset. The negative delay values for our wild-type cells likely reflect small differences
482 in experimental design compared to the study by (Lackner et al., 2021).
483 **D** Expression of naïve pluripotency marker genes in 2i (open circles) and after 24 h differentiation in
484 N2B27 (dots) in wild-type versus *Med12*-mutant cells. Relative expression values shown as log2(TPM),
485 error bars indicate standard deviation.
486 **E** Distribution of slopes of regulation (gene expression change over differentiation in wild type divided
487 by gene expression change over differentiation in *Med12* mutant) for the 100 genes with the strongest
488 negative (left panel) and positive (right panel) fold-change in wild-type and *Med12*-mutant cells. Bar
489 indicates median, boxes indicate 25th and 75th percentile.

490 Discussion

491 Here we use a *Spry4*$^{H2B\text{-}Venus}$ reporter to screen for regulators of developmental gene
492 expression in pluripotent stem cells. This screen returned components of the FGF/ERK and
493 the mTOR signaling systems that positively and negatively regulate reporter expression,
494 respectively, as well as several members of the Mediator and Elongator complexes. Focusing
495 on *Med12* we show that it cooperates with multiple signaling systems to regulate gene
496 expression in pluripotent cells. *Med12* was not required for the differentiation of Epi and PrE
497 identities, but dynamics of pluripotency transitions were impaired in *Med12*-mutant cells.
498 Together, these results suggest that *Med12* amplifies transcriptional changes in pluripotent
499 cells, possibly by contributing to Mediator's function in establishing promoter-enhancer
500 contacts (Kagey et al., 2010).
501 Previous genome-wide screens have used retention of clonogenicity or the continued
502 expression of pluripotency-associated reporter alleles in differentiation conditions as read-outs
503 to identify regulators of pluripotency and lineage transitions (Betschinger et al., 2013; Kagey
504 et al., 2010; M. Li et al., 2018; Villegas et al., 2019). In our study, the combination of a *Spry4*$^{H2B-}$
505 ^{Venus} allele with flow sorting constitutes a highly sensitive read-out that is focused on the activity
506 of specific signaling systems in pluripotent cells, and reliably detects new regulators even if
507 they have only small effect sizes. The screen's specificity shows in the strong representation
508 of genes involved in the FGF/ERK signaling cascade, from genes that encode synthetases for
509 FGF co-factors, over FGF receptors, to intracellular signaling genes. Surprisingly however, we
510 did not find any sequence-specific transcription factors downstream of FGF/ERK signaling in
511 our screen. This could be explained by the expression of multiple functionally redundant
512 FGF/ERK signaling effectors in pluripotent cells, or through previously proposed transcription
513 factor-independent regulation of RNA polymerase activity by ERK (Tee et al., 2014).

514 In addition to components of FGF and mTOR signaling systems, the screen returned several
515 members of the SWI/SNF and the Mediator complexes. The core Mediator complex is thought
516 to be required for the expression of most genes in eukaryotic genomes, but individual subunits
517 have been suggested to regulate gene expression downstream of specific signaling systems
518 such as the serum response network (Donner et al., 2010; Stevens et al., 2002), or Wnt
519 (Rocha et al., 2010). However, when we tested this idea for *Med12*, we found that its loss did
520 not phenocopy the effects of specific signaling perturbations. This finding suggests that
521 previously reported functional connections, such as the link between *Med12* and Wnt signaling
522 (Rocha et al., 2010), are strongly context-dependent.
523 *Med12* is a critical component of the Mediator-associated CDK8-module. In contrast to
524 pharmacological inhibition of CDK8 which has been reported to boost pluripotency similarly to
525 ERK signaling inhibition (Lynch et al., 2020), we find that loss of *Med12* leads to lower
526 expression levels of pluripotency markers. These opposing phenotypes indicate that MED12
527 has functions that are independent from the CDK8-module (Aranda-Orgilles et al., 2016). This
528 would also explain why we did not detect any other CDK8-module components in our screen.
529 Lynch et al. found that maintenance of pluripotency required the presence of CDK8, but
530 absence of its kinase activity. Another possible explanation for the opposing phenotypes of
531 CDK8 inhibition and *Med12* loss-of-function therefore is that MED12 participates in
532 assembling kinase-inactive CDK8 complexes that support pluripotency.
533 *Med12* has been found to maintain pluripotency not only in the epiblast, but also in the
534 trophoectoderm (Halstead et al., 2024). Its role to maintain pluripotency gene expression
535 reported here is supported by earlier studies which found that MED12 and NANOG proteins
536 interact, that MED12 and NANOG have similar DNA-binding profiles, and that MED12
537 promotes *Nanog* expression (Apostolou et al., 2013; Tutter et al., 2009). Several Mediator
538 subunits, including *Med12*, have been identified in a screen for pluripotency maintenance that
539 focused on transcription and chromatin regulators (Kagey et al., 2010). This study furthermore
540 suggested that interactions between Mediator and cohesin contribute to genome folding and
541 efficient enhancer-promoter interactions. When we probe *Med12* functions in lineage
542 transitions, we find that, in contrast to *Med24,* loss of *Med12* does not compromise PrE
543 differentiation (Hamilton et al., 2019). *Med12*-mutant cells however show a slower
544 downregulation of pluripotency genes and a decreased ability to revert to naïve pluripotency
545 in a colony-forming assay. We speculate that these cellular phenotypes are a reflection of a
546 reduced ability of *Med12*-mutant cells to reconfigure the chromatin upon changing signaling
547 environments. It is likely that the expression of individual genes is differentially sensitive to the
548 loss of *Med12*. This may be the reason why expression from the *Sprouty4* locus, which is the
549 most strongly upregulated gene upon acute FGF stimulation, shows a particularly high
550 sensitivity to loss of *Med12*. In line with this idea, requirements of *Med12* for efficient induction

551 are not exclusive to endogenous genes, but extend to exogenous transgenes such as the
552 inducible GATA6-mCherry construct used to trigger primitive endoderm differentiation in our
553 study. Surprisingly, such differential quantitative defects in the regulation of single genes upon
554 loss of *Med12* do not lead to strong defects in acquiring early differentiated fates, such that
555 transcriptomes of individual differentiated cells are not systematically different from each other
556 in *Med12*-mutant and wild-type cells. This suggests that intracellular regulatory networks can
557 buffer the composition of cellular transcriptomes against variable transcription efficiencies.

558 Acknowledgements

559 We thank Kristin Nowak for generating *Fgf4*-mutant E14tg2a mESC lines, members of the
560 Imig lab for help with lentivirus production, and the protein chemistry facility of the MPI
561 Dortmund for supply of LIF and enzymes for molecular biology. Michelle Marten provided
562 technical and organizational support for tissue culture and flow sorting throughout the project.
563 We thank members of the Schröter lab, the Department of Systemic Cell Biology, Jochen Imig
564 and Cristina Pina for critical discussions and feedback on earlier versions of the manuscript.

565 Declaration of interest

566 The authors declare that they have no conflict of interest.

Materials and Methods

Cell culture

Routine culture of mESCs was performed at 37 °C with 5% CO_2 in either serum + LIF medium (ESL, composed of GMEM with 10% fetal bovine serum (FBS), 2 mM GlutaMAX, 1 mM sodium pyruvate, 0.1 mM b-mercaptoethanol and 10 ng/mL LIF), on 0.1% gelatine coated dishes, or in 2i + LIF medium on fibronectin coated dishes. 2i + LIF is N2B27 supplemented with 1 µM PD0325901 (SelleckChem), 3 µM CHIR99201 (Tocris) and 10 ng/ml LIF (protein chemistry facility, MPI Dortmund). N2B27 was prepared as a 1:1 mixture of DMEM/F12 and Neuropan Basal Medium (both from PAN Biotech), supplemented with 1X N2 and 1X B27 supplements, 1X L-Glutamax, 0.0025% BSA, and 0.2 mM ß-mercaptoethanol (all from ThermoFisher). *Fgf4*-mutant cell lines were cultured in 2i + LIF supplemented with 10% FBS. Cells were passaged every two to three days, and detached with trypsin (PAN Biotech) or Accutase (Sigma-Aldrich).

Cell lines

All cell lines generated in this study were derived from the E14tg2a wild-type line (Hooper et al., 1987). The GATA4-mCherry inducible line used for single cell RNA sequencing has been described previously (Raina et al., 2021). The *Spry4*$^{H2B\text{-}Venus/+}$-reporter line was generated with a previously described targeting construct (Morgani et al., 2018) using lipofectamine 2000 according manufacturer's instructions (Thermo Fisher Scientific). Correctly targeted clones were identified via long-range PCR as described in (Morgani et al., 2018). GATA6-mCherry inducible lines were established as described for GATA4-mCherry inducible lines in (Raina et al., 2021), but replacing the *Gata4* with a *Gata6* coding sequence in the PiggyBac vector for inducible gene expression. We established multiple clonal lines and tested them for GATA6-mCherry induction levels upon dox-treatment by flow cytometry. Three independent clones with induction levels similar or slightly higher than the previously established GATA4-mCherry inducible lines were selected for the experiment shown in Fig. 5D, and a single clonal line was chosen for all other experiments, including mutagenesis of *Med12*. Newly generated *Spry4*$^{H2B\text{-}Venus/+}$-reporter and GATA6-mCherry inducible cell lines were checked for karyotypic abnormalities. To label nuclei for time lapse imaging cells were transfected with pCX-H2B-Cerulean- IRES-puro (Schumacher et al., 2024). Cell lines carrying PiggyBac transgenes were kept under appropriate selection to prevent transgene repression over passaging.

598 # sgRNA cloning and generation of single-gene mutants

599 For mutagenesis of individual genes via CRISPR/Cas9, gene targeting sgRNAs (Supp
600 Table 7) were cloned into pX459 (Addgene plasmid #48139) using BbsI (NEB) overhangs
601 following Ran et al., 2013 (Ran et al., 2013). Clonal mutant lines were generated using a
602 combination of sgRNAs with targeting sequences 100 to 200 bp apart in the genome. Single
603 sgRNAs were used when generating polyclonal lines. For validation experiments of the
604 CRISPR screen (Figs. 1 and 2), we selected the most enriched sgRNA in sorted cells. A total
605 of 1 µg of sgRNA containing px459 vectors was mixed with a final concentration of 0.04 µg/ml
606 Lipofectamine 2000 (Thermo Fisher Scientific) in Opti-MEM (Gibco) according to the
607 manufacturer's protocol. For the generation of clonal lines, cells were seeded at clonal density
608 into 10 cm dishes after transfection, for polyclonal experiments approximately 50k cells/cm^2
609 were seeded. To enrich for successfully transfected cells, selection with 1.5 µg/ml puromycin
610 was started 24 h after transfection for 48 h. To establish clonal lines, single-cell derived
611 colonies were picked 4 to 6 d after transfection and expanded. For molecular characterization
612 of genetic lesions, genomic DNA was purified with Terra™ PCR Direct Genotyping Kit
613 (Takara), followed by PCR amplification and Sanger sequencing of specific genomic regions
614 encompassing the target site.
615

616 # Genome-wide CRISPR Screen

617 To generate stably CAS9-expressing *Spry4*$^{H2B\text{-}Venus/+}$ reporter cells, cells were transduced with
618 lentiCas9-Blast lentiviral particles (Addgene #52962-LV) at a multiplicity of infection of
619 approximately 0.1. Transduction was performed with attached cells, 20 h after seeding at 20
620 000 cells/cm^2, in presence of 5 µg/ml Polybrene in ESL. Continuous blasticidin (15 µg/ml,
621 Gibco) selection was started 24 h after transduction. Lentiviral particles of the genome-wide
622 gRNA library Brie (Addgene #73633) were generated according to standard protocols (Doench
623 et al., 2016). For library transduction, 150 * 10^6 CAS9-expressing *Spry4*$^{H2B\text{-}Venus/+}$ reporter cells
624 were detached and mixed with the virus library in ESL with 5 µg/ml Polybrene. The following
625 day, the same number of cells was reseeded and put under selection with puromycin (1.5
626 µg/ml, Sigma-Aldrich). Comparing cell counts with and without selection indicated a
627 transduction efficiency of 25%, resulting in a >400-fold coverage of transduced cells per gRNA.
628 In all subsequent steps, at least 31 * 10^6 cells were processed to maintain gRNA coverage.
629 To identify gRNAs enriched in cell populations with high and low *Spry*4:H2B-Venus
630 expression, at least 0.5 * 10^6 cells with the lowest or highest 1% of *Spry*4:H2B-Venus
631 fluorescence, or 3 * 10^6 cells with the lowest or highest 5% of *Spry*4:H2B-Venus fluorescence
632 were FAC sorted and their DNA isolated by column-based genomic DNA purification (Monarch

633 Genomic DNA Purification Kit, NEB). For reference, the genomic DNA of 31 * 10^6 non-sorted
634 control cells was purified in parallel. The integrated gRNA was PCR amplified using Pfu
635 polymerase (prepared in house) with a sample specific, sequencing adapter and index
636 containing primers (Supp Table 7; Carlini et al., 2021) using the complete purified genomic
637 DNA as template. PCR-samples were purified with the SPRIselect reagent (Beckman Coulter)
638 with double-sided size selection. Briefly, 0.5x SPRIselect was added to each sample,
639 incubated for 5 min at RT and the SPRIselect removed with a magnet. This supernatant was
640 again mixed with 1.2x SPRIselect, incubated and then discarded. After washing the beads,
641 the DNA library was eluted from the beads and used for sequencing.
642 Paired-End Illumina Sequencing with a read length of 150 bp pairs was performed with at least
643 10 * 10^6 reads per sorted sample and 30 * 10^6 reads for the unsorted library controls. The raw
644 reads were trimmed using Cutadapt (Martin, 2011) to remove the vector binding sequence.
645 The reads were mapped to individual gRNAs, counted using *norm-method total* and
646 statistically tested on the targeted gene levels using *gene-lfc-method alphamean* with Mageck
647 (W. Li et al., 2014). Hits were selected based on the false discovery rate.
648

649 # Immunostaining

650 Immunostaining was performed as previously described (Schröter et al., 2015), Briefly, cells
651 were washed with PBS containing Calcium and Magnesium, followed by fixation with 4%
652 paraformaldehyde (Histofix, Sigma-Aldrich) for 15 min. Cells were permeabilized and blocked
653 by rinsing and washing three times with PBS with 0.1% Triton X-100 and 1.0% bovine serum
654 albumin (PBT-BSA). Primary antibodies (Anti-mouse NANOG (Affymetrix eBioscience,
655 Cat.:14-5761), Anti-SOX17 (R&D systems, Cat.: AF1924), anti-Oct3/4 (POU5F1, Santa Cruz
656 Biotechnology, Cat:. sc-5279)) were diluted 1:200 in PBT-BSA and incubated with the cells
657 overnight at 4 °C. The next day, cells were washed in PBT-BSA and incubated with Alexa
658 Fluor-conjugated secondary antibodies at 4 µg/ml (Invitrogen/Life Technologies) and Hoechst
659 33342 at 1 µg/ml (Invitrogen) in PBT-BSA in the dark for 2 h. Finally, samples were rinsed and
660 washed with PBS and imaged in a mounting medium consisting of 80% glycerol, 16% PBS
661 and 4% n-propyl-gallate.
662

663 # Immunoblotting

664 For western blot analysis of MED12 and ppERK, cells were washed twice with ice-cold PBS,
665 supplemented with 1 mM activated orthovanadate in case of ppERK detection. Cells were
666 mechanically detached in lysis buffer, based on commercially available lysis buffer (Cell
667 Signaling) supplemented with benzonase (Sigma-Aldrich), cOmplete EDTA-free protease

668 inhibitor cocktail (Roche), phosphate inhibitors P1 and P2 (Sigma). The lysates were snap
669 frozen in liquid nitrogen twice and centrifuged. Protein concentration in the supernatant was
670 measured with a micro BCA assay (Thermo Scientific). For western analysis, 20 µg of protein
671 per sample were denatured by adding 5x Laemelli buffer and incubation at 95 °C for 5 min.
672 The SDS-PAGE was run in 1x MOPS buffer (ThermoFisher) with 5 mM sodium-bisulfate and
673 immediately transferred onto methanol-activated PVDF membranes. Transfer was performed
674 in transfer buffer (12mM Tris-Base, 96mM Glycine, 20% methanol) at 40 V for 1.5 h in a
675 NuPage transfer system (ThermoFisher). Membranes were blocked at RT for 1 h in Intercept
676 blocking buffer (LI-COR), which was also used for the dilution and incubation with the primary
677 antibodies anti-Tubulin 1:10000 (T6074, Sigma), anti-pERK1/2 1:1000 (4370S, Cell
678 Signaling), anti-total ERK1/2 1:1000 (ab36991, Abcam) or anti-Med12 (1:250, A300-774A,
679 Bethyl Laboratories). Appropriate secondary antibodies (IRdyes, LI-COR) were used at a
680 dilution of 1:5000. Blots were imaged on an Odyssey CLx (LI-COR). Quantification of ppERK
681 bands was performed using the gel quantification tool in Fiji, using the combined intensities of
682 ERK1 and ERK2 bands, and normalizing ppERK by total ERK signals.
683

684 # In situ HCR

685 In situ hybridization probes against Spry4 and Nanog were designed by, and all commercial
686 reagents for the staining procedure were obtained from Molecular Instruments, if not indicated
687 otherwise. mRNAs were stained in solution as previously reported (Choi et al., 2018).
688 Specifically, cells from confluent 6-well plate wells were washed with PBS and detached using
689 trypsin. Following centrifugation for 5 min at 200xg, the specification for all further
690 centrifugation steps, cells were fixed with 4% PFA for 1 h. After removal of the fixative via
691 centrifugation, cells were washed four times with PBS with 0.1% Tween20 (PBST, Bio-Rad).
692 Cells were incubated overnight in ice-cold ethanol. Starting with 1 * 10^6 cells, and two
693 additional washes with PBST, cells were incubated in 400 µl probe hybridization buffer for
694 30 min at 37 °C. 2 pmol of gene-specific hairpins were prepared in 100 µl preheated probe
695 hybridization buffer and added to the cell suspension, which was subsequently incubated
696 overnight at 37 °C. Preheated wash buffer was used to remove residual hybridization oligos
697 by washing thrice with 10 min of intermediate incubation. One final wash and 5 min incubation
698 were performed in saline-sodium citrate (SSC, Sigma-Aldrich) buffer with 0.1% Tween20.
699 Cells were resuspended in 150 µl amplification buffer. 10 pmol of each labeled hairpin were
700 mixed, heated to 95 °C for 90 s, and cooled back to RT. Hairpins were added into 100 µl of
701 amplification buffer, mixed with the cell suspension and incubated in the dark for 1 h. A final
702 five washes with SCCT were followed by mounting the sample onto a microscopy glass slide.
703 Samples were resuspended in 20 to 100 µl SCCT to ensure high single-cell densities. 2 µl of

704 the cell suspension were squished between the slide and a cover slip to maximize area per
705 cell and distance between mRNA spots.
706

707 RNA labeling

708 Newly synthesized RNA was labelled using the Click-iT™ RNA Alexa Fluor™ 594 Imaging Kit
709 (Invitrogen) according to the manufactures protocol. Briefly, we incubated cells with 1 mM 5-
710 ethynyl uridine for the last 30 min or 1h of differentiation or during pluripotency. After, washing,
711 fixation with 4% PFA and permeabilization, the click reaction with the Alexa Fluor 594 azide
712 was performed for 30 min, followed by washing and nuclear staining with SiR-DNA 647
713 (Spirochrome) for 15 min.
714

715 Imaging and Image Analysis

716 Tilescans of immunostainings were imaged with a Leica SP8 confocal microscope (Leica
717 Microsystems) with a 63x 1.4 NA oil immersion objective. Images were analyzed in Fiji
718 (Schindelin et al., 2012). For segmentation, StarDist 2D (Schmidt et al., 2018) was used using
719 the versatile (fluorescent nuclei) model and default post processing parameters. Mean
720 fluorescence intensity was measured in segmented cells in all acquired channels. Cells with
721 a nuclear area smaller than 40 μm^2 were filtered out. To determine fluorescence intensity
722 threshold values for the classification of cell types, we manually selected thresholds that best
723 bisected the bimodal expression profiles of the lineage markers. The same thresholds were
724 applied to different samples in a single experiment. In the RNA-labeling experiment, after
725 segmentation based on the nuclear staining and intensity measurement, a gaussian mixture
726 model was fitted to the intensity distributions of the H2B-Cerulean channel. Using the posterior
727 probability, the fluorescence intensity thresholds at which a cell can be assigned to the correct
728 genotype with an ≥ 85% certainty were determined and genotype assignment was performed
729 accordingly, not assigning cells in between the populations. The integrated intensity of the
730 RNA-AF594 signal within the nucleus region was used to determine the amount of newly
731 produced RNA within the labeling period.
732 Images of live *Spry4*$^{H2B\text{-}Venus/+}$-reporter cells were acquired with an Olympus IX81 widefield
733 microscope, equipped with a stage top incubator (ibidi), pE4000 illumination (CoolLED),
734 ORCA-Quest qCMOS camera (Hamamatsu) with a 63x 1.35 NA oil immersion objective.
735 Hardware was controlled by Olympus CellSens Software. Images of in situ HCR for mRNA
736 counting were acquired on the same system with a 100x 1.4 NA objective with 1024x1024
737 pixels and at least 20 z-slices, separated by 0.4 µm. Single cells were manually segmented
738 on a brightfield image, taken in the middle of the z-stack. Counting mRNA spots from in situ

739 HCR was performed using RS-FISH (Bahry et al., 2022). The anisotropy was determined from
740 single spots and set to 1.2. No robust fitting was applied. Sigma was set to 0.994. The
741 threshold, the image maximum and the minimal spot intensity threshold were set for each
742 channel per replicate manually, to account for different (background) intensity levels. Time
743 lapse imaging was performed with a 40x 0.9 NA objective on an Olympus IX81 widefield
744 microscope, equipped with an LED-based illumination system (pE4000, CoolLED) and an iXon
745 888 EM-CCD camera (Andor). MicroManager (Edelstein et al., 2010) was used to control the
746 hardware. Images were taken every 10 min. Tracking was performed with the manual tracking
747 function in Trackmate v7 (Ershov et al., 2022) and fluorescence intensity was measured as
748 the mean intensity in a spot with a 4 µm radius within the nucleus. In R, tracks were smoothed
749 with a rolling average over 7 frames. For ROC analysis the R package pROC (Robin et al.,
750 2011) was applied and the optimal threshold was defined by the Youden's J statistic (Youden,
751 1950).
752

753 # Flow cytometry

754 Analysis of *Spry4*:H2B-Venus reporter expression in live or fixed cells was performed on a
755 LSRII flow cytometer (BD Biosciences). Cell sorting and analysis of GATA6-mCherry
756 expression was carried out using a FACS Aria Fusion (BD Biosciences). Primary data analysis
757 including gating single cells based on SSC and FSC was done with FlowJo version 9 (BD
758 Biosciences).
759

760 # Clonogenicity Assay

761 Clonogenicity assays were performed according to (Kalkan et al., 2017). Briefly, 1 * 10^4
762 cells/cm^2 were seeded in 2i + LIF for 24 h, followed by differentiation in N2B27 for 48 h. Control
763 wells for each parental cell line were kept in 2i + LIF. Cells were then detached with Accutase
764 to single cells, and 500 cells were reseeded into 6-well plates with 2i + LIF + 10% FBS. 10%
765 FBS were included to support survival of *Fgf4*-mutant cells.
766 After 5 d, the colonies formed were fixed and stained with an alkaline phosphatase assay kit
767 (Sigma-Aldrich) to distinguish pluripotent and differentiated colonies. Tile scans of the wells
768 were acquired with an Olympus IX81 widefield microscope with a 4x 0.16 NA objective. We
769 applied background subtraction, gaussian blurring, Otsu-thresholding, and conversion of
770 images to a binary mask in ImageJ, and then used the *AnalyzeParticles* function to set
771 thresholds for size and circularity and to determine the number of colonies. Colony numbers
772 were normalized to the number of colonies obtained in the control.
773

774 # Bulk RNA sequencing

775 For bulk RNA sequencing, cells were seeded at a density between 3.5 and 5.5 * 10^4 cells/cm^2
776 in 2i or N2B27 + Chiron + LIF, followed by stimulation under indicated conditions. Replicates
777 were obtained either from independent biological experiments (Fig. 3 A, B) or from both
778 independent biological experiments and independent *Med12*-mutant lines (Fig. 3F, G). RNA
779 isolation was performed with TRIzol (ambion) according to the manufacturer's instructions.
780 Sequencing libraries were prepared on polyA-enriched RNAs, followed by paired-end
781 sequencing at a read-length of 150 bp and depth of approximately 30 * 10^6 reads per sample.
782 Strand-specific libraries were generated only for the FGF-titration experiment (Fig. 1 Supp 1)
783 and the differentiation of the *Med12* wild-type and mutant cells (Fig. 3A, B). Raw reads were
784 mapped to the mouse genome (GRCm39, release 108 (both *Med12* mutant experiments) or
785 release 97 (FGF titration experiment) with hisat2 (v2.1.0; Kim et al., 2019). SeqMonk was used
786 to quantify counts per gene, either as TPM or as raw counts as input for downstream DESeq2
787 analysis (Love et al., 2014) for identification of differentially expressed genes.
788 Differentiation delay in Med12 mutants was estimated according to (Lackner et al., 2021). We
789 first determined the expression change of the naïve marker genes *Nanog*, *Esrrb*, *Tbx3*,
790 *Tfcp2l1*, *Klf4*, *Prdm14* and *Zfp4* in *Med12*-mutant and wild-type cells, and then plotted the
791 Euclidean distance of this expression change to that of the time-resolved dataset from Lackner
792 et al., 2021.
793 Signaling footprint analysis in *Med12* mutants was performed similarly to Lacker et al., 2021.
794 This study defined a specific set of target genes for each pluripotency associated signaling
795 system based on gene expression changes in knockouts of signaling genes. A signaling
796 footprint for a knockout line can then be determined from the difference in the expression of
797 pathway footprint genes to the wild-type line after 24 h of differentiation. Measures for the
798 signaling footprint are the Spearman correlation between each knockout line and the
799 respective pathway defining knockout, and the ratio between the sum of expression fold
800 changes between a knockout line and the respective pathway defining knockout, defined as
801 pathway activity. To compare the *Med12* mutant data from this study, the wild type conditions
802 were used for batch correction.
803

804 # Cell multiplexing and scRNA sequencing

805 Cells for scRNAseq were seeded at a density of 3.5 * 10^4 cells/cm^2 in 6-well plates in 2i + LIF
806 and grown overnight. The next morning, induction in 2i + LIF + dox was first started in the
807 mutant clones, and 4 h later in the wild-type lines. After 8h and 4 h, respectively, induction was
808 stopped by washing once with N2B27, followed by 20 h of differentiation in N2B27. Controls

809 for each cell line were continuously kept in 2i + LIF. For sequencing, cells were washed three
810 times with PBS and detached with Accutase. Accutase was removed by centrifugation and 1
811 * 10^6 cells per sample were resuspended in PBS + 0.04 % BSA and immediately used for
812 multiplexing labeling following the protocol of 10x Genomics for samples with a viability above
813 80 % (Cell Multiplexing Oligo Labeling for Single Cell RNA Sequencing Protocols with Feature
814 Barcode technology, CG000391). Briefly, cells were spun down once again, resuspended with
815 individual cell multiplexing oligos (CMO no. 301 to 310) and incubated for 5 min at RT. Cells
816 were washed twice with PBS + 1 % BSA and passed through a cell strainer (FALCON, mesh
817 size 35 µm). A total of 1.2 * 10^5 single cells from all samples were pooled at equal ratios, and
818 4 * 10^4 were used for droplet generation, corresponding to a target number of 2.4 * 10^4 cell-
819 containing droplets. Droplet generation, lysis, mRNA and cell barcode capture, and generation
820 of both the gene expression library as well as the cell multiplexing library was performed
821 following the instructions by 10x genomics (Chromium Next GEM Single Cell 3' Reagent Kits
822 v3.1 (Dual Index) with Feature Barcode technology for Cell Multiplexing, CG000388).
823 Specifically, we chose 11 PCR cycles for cDNA amplification and 10 cycles for the sample
824 index PCR. Concentration and insert size distribution for both the gene expression library and
825 the cell multiplexing library were determined with a BioAnalyzer High Sensitivity DNA Assay
826 (Agilent). Sequencing was performed on a NovaSeq 6000 on multiple flowcells with a paired-
827 end 150 bp configuration. In total 1.2 * 10^9 and 2.3 * 10^8 read pairs were obtained for the gene
828 expression and multiplexing library, respectively.
829 Demultiplexing to the individual samples, based on the cell multiplexing barcode and
830 alignment to the mouse genome mm10 (GENCODE vM23/Ensembl 98, obtained from 10x
831 Genomics) was performed with CellRanger (version 7.1.0, 10x Genomics). Downstream
832 analysis was performed in R with Seurat v5 (Hao et al., 2023). We first filtered cells by
833 removing barcodes with ≤ 2500 detected genes and ≥15 % of reads aligned to mitochondrial
834 genes, retaining between 1100 and 1700 cells per sample with median mRNA counts per cell
835 between 23233 and 27890 in the different samples. mRNA counts for each gene were
836 normalized by dividing its counts by the total number of counts per cell, multiplied by 10000.
837 Log1p transformation was applied before plotting expression data as violin plots. For
838 downstream analysis and representation of gene expression as heatmaps, centering counts
839 for each feature and scaling to its standard deviation was applied. Principal component
840 analysis was performed on the 2000 most variable features in the relevant subset of cells. The
841 resolution of the Louvain clustering algorithm was set to 0.05 when clustering multiple
842 samples. In case of Jaccard-Index estimation the clustering resolution was set to 0.15 and the
843 clustering was performed on each sample separately. 100-fold repetition of this clustering
844 approach with a random subset of the data with 70 % of the cells allowed the calculation of a
845 Jaccard-index, as previously described (Tang et al., 2021). For annotation of the Epi- and PrE-

fate, the cells of the differentiated samples were integrated with Seurat integration based on the *rpca* reduction. Differentially expressed genes between cell states and genotypes were identified with the *FindMarkers* function in Seurat with a minimal expression difference in the log1p transformed expression values of 0.5. Biological noise was quantitated and distinguished from modeled technical noise in local neighborhoods of each cell with VarID2 (Rosales-Alvarez et al., 2023).

Data and code availability

Sequencing data from this paper has been deposited at GEO with accession number GSE253609. All code used for analysis and visualization, together with a list of the R packages used, is available from the authors upon request.

Bibliography

Apostolou, E., Ferrari, F., Walsh, R. M., Bar-Nur, O., Stadtfeld, M., Cheloufi, S., Stuart, H. T., Polo, J. M., Ohsumi, T. K., Borowsky, M. L., Kharchenko, P. V., Park, P. J., & Hochedlinger, K. (2013). Genome-wide chromatin interactions of the nanog locus in pluripotency, differentiation, and reprogramming. *Cell Stem Cell*, *12*(6), 699–712. https://doi.org/10.1016/j.stem.2013.04.013

Aranda-Orgilles, B., Saldaña-Meyer, R., Wang, E., Trompouki, E., Fassl, A., Lau, S., Mullenders, J., Rocha, P. P., Raviram, R., Guillamot, M., Sánchez-Díaz, M., Wang, K., Kayembe, C., Zhang, N., Amoasii, L., Choudhuri, A., Skok, J. A., Schober, M., Reinberg, D., … Aifantis, I. (2016). MED12 Regulates HSC-Specific Enhancers Independently of Mediator Kinase Activity to Control Hematopoiesis. *Cell Stem Cell*, *19*(6), 784–799. https://doi.org/10.1016/j.stem.2016.08.004

Athanasouli, P., Balli, M., De Jaime-Soguero, A., Boel, A., Papanikolaou, S., van der Veer, B. K., Janiszewski, A., Vanhessche, T., Francis, A., El Laithy, Y., Nigro, A. Lo, Aulicino, F., Koh, K. P., Pasque, V., Cosma, M. P., Verfaillie, C., Zwijsen, A., Heindryckx, B., Nikolaou, C., & Lluis, F. (2023). The Wnt/TCF7L1 transcriptional repressor axis drives primitive endoderm formation by antagonizing naive and formative pluripotency. *Nature Communications*, *14*(1), 1–19. https://doi.org/10.1038/s41467-023-36914-1

Bahry, E., Breimann, L., Zouinkhi, M., Epstein, L., Kolyvanov, K., Mamrak, N., King, B., Long, X., Harrington, K. I. S., Lionnet, T., & Preibisch, S. (2022). RS-FISH: precise, interactive, fast, and scalable FISH spot detection. *Nature Methods*, *19*(12), 1563–1567. https://doi.org/10.1038/s41592-022-01669-y

Betschinger, J., Nichols, J., Dietmann, S., Corrin, P. D., Paddison, P. J., & Smith, A. (2013). Exit from pluripotency is gated by intracellular redistribution of the bHLH transcription factor Tfe3. *Cell*, *153*(2), 335–347. https://doi.org/10.1016/j.cell.2013.03.012

Carlini, V., Gretarsson, K. H., & Hackett, J. A. (2021). Genome-scale CRISPR screening for regulators of cell fate transitions. In *Methods in Molecular Biology* (Vol. 2214, pp. 91–108). Humana Press Inc. https://doi.org/10.1007/978-1-0716-0958-3_7

Chazaud, C., & Yamanaka, Y. (2016). Lineage specification in the mouse preimplantation embryo. *Development*, *143*(7), 1063–1074. https://doi.org/10.1242/DEV.128314

Doench, J. G., Fusi, N., Sullender, M., Hegde, M., Vaimberg, E. W., Donovan, K. F., Smith, I., Tothova, Z., Wilen, C., Orchard, R., Virgin, H. W., Listgarten, J., & Root, D. E. (2016). Optimized sgRNA design to maximize activity and minimize off-target effects of CRISPR-Cas9. *Nature Biotechnology*, *34*(2), 184–191. https://doi.org/10.1038/nbt.3437

Donner, A. J., Ebmeier, C. C., Taatjes, D. J., & Espinosa, J. M. (2010). CDK8 is a positive regulator of transcriptional elongation within the serum response network. *Nature Structural and Molecular Biology*, *17*(2), 194–201. https://doi.org/10.1038/nsmb.1752

Edelstein, A., Amodaj, N., Hoover, K., Vale, R., & Stuurman, N. (2010). Computer control of microscopes using μManager. *Current Protocols in Molecular Biology*, *Chapter 14*. https://doi.org/10.1002/0471142727.MB1420S92

Ershov, D., Phan, M. S., Pylvänäinen, J. W., Rigaud, S. U., Le Blanc, L., Charles-Orszag, A., Conway, J. R. W., Laine, R. F., Roy, N. H., Bonazzi, D., Duménil, G., Jacquemet, G., & Tinevez, J. Y. (2022). TrackMate 7: integrating state-of-the-art segmentation algorithms into tracking pipelines. *Nature Methods*, *19*(7), 829–832. https://doi.org/10.1038/s41592-022-01507-1

Fujikura, J., Yamato, E., Yonemura, S., Hosoda, K., Masui, S., Nakao, K., Miyazaki, J. I., & Niwa, H. (2002). Differentiation of embryonic stem cells is induced by GATA factors. *Genes & Development*, *16*(7), 784–789. https://doi.org/10.1101/GAD.968802

Halstead, M. M., Goad, J., Khan, A., Deshmukh, R., & Rajkovic, A. (2024). Maternal Med12 safeguards trophoblast pluripotency and placental development. *BioRxiv*, 2024.11.01.621455. https://doi.org/10.1101/2024.11.01.621455

Hamilton, W. B., Mosesson, Y., Monteiro, R. S., Emdal, K. B., Knudsen, T. E., Francavilla, C., Barkai, N., Olsen, J. V., & Brickman, J. M. (2019). Dynamic lineage priming is driven via direct enhancer regulation by ERK. *Nature*, *575*(7782), 355–360. https://doi.org/10.1038/s41586-019-1732-z

Hanna, R. E., & Doench, J. G. (2020). Design and analysis of CRISPR–Cas experiments. *Nature Biotechnology*, *38*(7), 813–823. https://doi.org/10.1038/s41587-020-0490-7

Hao, Y., Stuart, T., Kowalski, M. H., Choudhary, S., Hoffman, P., Hartman, A., Srivastava, A., Molla, G., Madad, S., Fernandez-Granda, C., & Satija, R. (2023). Dictionary learning for integrative, multimodal and scalable single-cell analysis. *Nature Biotechnology*, 1–12. https://doi.org/10.1038/s41587-023-01767-y

Hooper, M., Hardy, K., Handyside, A., Hunter, S., & Monk, M. (1987). HPRT-deficient (Lesch-Nyhan) mouse embryos derived from germline colonization by cultured cells. *Nature*, *326*(6110), 292–295. https://doi.org/10.1038/326292A0

Kagey, M. H., Newman, J. J., Bilodeau, S., Zhan, Y., Orlando, D. A., Van Berkum, N. L., Ebmeier, C. C., Goossens, J., Rahl, P. B., Levine, S. S., Taatjes, D. J., Dekker, J., & Young, R. A. (2010). Mediator and cohesin connect gene expression and chromatin architecture. *Nature*, *467*(7314), 430–435. https://doi.org/10.1038/nature09380

Kalkan, T., Bornelöv, S., Mulas, C., Diamanti, E., Lohoff, T., Ralser, M., Middelkamp, S., Lombard, P., Nichols, J., & Smith, A. (2019). Complementary Activity of ETV5, RBPJ, and TCF3 Drives Formative Transition from Naive Pluripotency. *Cell Stem Cell*, *24*(5), 785–801. https://doi.org/10.1016/j.stem.2019.03.017

Kalkan, T., Olova, N., Roode, M., Mulas, C., Lee, H. J., Nett, I., Marks, H., Walker, R., Stunnenberg, H. G., Lilley, K. S., Nichols, J., Reik, W., Bertone, P., & Smith, A. (2017). Tracking the embryonic stem cell transition from ground state pluripotency. *Development*, *144*(7), 1221–1234. https://doi.org/10.1242/dev.142711

934 Kalkan, T., & Smith, A. (2014). Mapping the route from naive pluripotency to lineage
935 specification. *Philosophical Transactions of the Royal Society B: Biological Sciences*,
936 *369*(1657). https://doi.org/10.1098/RSTB.2013.0540
937 Kang, M., Piliszek, A., Artus, J., & Hadjantonakis, A. K. (2013). FGF4 is required for lineage
938 restriction and salt-and-pepper distribution of primitive endoderm factors but not their
939 initial expression in the mouse. *Development*, *140*(2), 267–279.
940 https://doi.org/10.1242/DEV.084996
941 Kim, D., Paggi, J. M., Park, C., Bennett, C., & Salzberg, S. L. (2019). Graph-based genome
942 alignment and genotyping with HISAT2 and HISAT-genotype. *Nature Biotechnology*,
943 *37*(8), 907–915. https://doi.org/10.1038/S41587-019-0201-4
944 Knuesel, M. T., Meyer, K. D., Donner, A. J., Espinosa, J. M., & Taatjes, D. J. (2009). The
945 human CDK8 subcomplex is a histone kinase that requires Med12 for activity and can
946 function independently of mediator. *Molecular and Cellular Biology*, *29*(3), 650–661.
947 https://doi.org/10.1128/MCB.00993-08
948 Lackner, A., Sehlke, R., Garmhausen, M., Giuseppe Stirparo, G., Huth, M., Titz-Teixeira, F.,
949 Lelij, P., Ramesmayer, J., Thomas, H. F., Ralser, M., Santini, L., Galimberti, E., Sarov,
950 M., Stewart, A. F., Smith, A., Beyer, A., & Leeb, M. (2021). Cooperative genetic networks
951 drive embryonic stem cell transition from naïve to formative pluripotency. *The EMBO*
952 *Journal*, *40*(8). https://doi.org/10.15252/embj.2020105776
953 Li, M., Yu, J. S. L., Tilgner, K., Ong, S. H., Koike-Yusa, H., & Yusa, K. (2018). Genome-wide
954 CRISPR-KO Screen Uncovers mTORC1-Mediated Gsk3 Regulation in Naive
955 Pluripotency Maintenance and Dissolution. *Cell Reports*, *24*(2), 489–502.
956 https://doi.org/10.1016/j.celrep.2018.06.027
957 Li, W., Xu, H., Xiao, T., Cong, L., Love, M. I., Zhang, F., Irizarry, R. A., Liu, J. S., Brown, M.,
958 & Liu, X. S. (2014). MAGeCK enables robust identification of essential genes from
959 genome-scale CRISPR/Cas9 knockout screens. *Genome Biology*, *15*(554), 1–12.
960 https://doi.org/10.1186/s13059-014-0554-4
961 Love, M. I., Huber, W., & Anders, S. (2014). Moderated estimation of fold change and
962 dispersion for RNA-seq data with DESeq2. *Genome Biology*, *15*(12), 1–21.
963 https://doi.org/10.1186/s13059-014-0550-8
964 Luyties, O., & Taatjes, D. J. (2022). The Mediator kinase module: an interface between cell
965 signaling and transcription. *Trends in Biochemical Sciences*, *47*(4), 314–327.
966 https://doi.org/10.1016/j.tibs.2022.01.002
967 Lynch, C. J., Bernad, R., Martínez-Val, A., Shahbazi, M. N., Nóbrega-Pereira, S., Calvo, I.,
968 Blanco-Aparicio, C., Tarantino, C., Garreta, E., Richart-Ginés, L., Alcazar, N., Graña-
969 Castro, O., Gómez-Lopez, G., Aksoy, I., Muñoz-Martín, M., Martinez, S., Ortega, S.,
970 Prieto, S., Simboeck, E., … Serrano, M. (2020). Global hyperactivation of enhancers
971 stabilizes human and mouse naive pluripotency through inhibition of CDK8/19 Mediator
972 kinases. *Nature Cell Biology*, *22*(10), 1223–1238. https://doi.org/10.1038/s41556-020-
973 0573-1
974 Martin, M. (2011). Cutadapt removes adapter sequences from high-throughput sequencing
975 reads. *EMBnet.Journal*, *17*(1), 10–12. https://doi.org/10.14806/EJ.17.1.200
976 Morgani, S. M., & Brickman, J. M. (2015). LIF supports primitive endoderm expansion during
977 pre-implantation development. *Development*, *142*(20), 3488–3499.
978 https://doi.org/10.1242/DEV.125021
979 Morgani, S. M., Saiz, N., Garg, V., Raina, D., Simon, C. S., Kang, M., Arias, A. M., Nichols, J.,
980 Schröter, C., & Hadjantonakis, A. K. (2018). A Sprouty4 reporter to monitor FGF/ERK

signaling activity in ESCs and mice. *Developmental Biology*, *441*(1), 104–126. https://doi.org/10.1016/j.ydbio.2018.06.017

Neagu, A., van Genderen, E., Escudero, I., Verwegen, L., Kurek, D., Lehmann, J., Stel, J., Dirks, R. A. M., van Mierlo, G., Maas, A., Eleveld, C., Ge, Y., den Dekker, A. T., Brouwer, R. W. W., van IJcken, W. F. J., Modic, M., Drukker, M., Jansen, J. H., Rivron, N. C., … ten Berge, D. (2020). In vitro capture and characterization of embryonic rosette-stage pluripotency between naive and primed states. *Nature Cell Biology*, *22*(5), 534–545. https://doi.org/10.1038/S41556-020-0508-X

Nichols, J., Silva, J., Roode, M., & Smith, A. (2009). Suppression of Erk signalling promotes ground state pluripotency in the mouse embryo. *Development*, *136*(19), 3215–3222. https://doi.org/10.1242/dev.038893

Nichols, J., & Smith, A. (2009). Naive and Primed Pluripotent States. In *Cell Stem Cell* (Vol. 4, Issue 6, pp. 487–492). https://doi.org/10.1016/j.stem.2009.05.015

Ornitz, D. M., & Itoh, N. (2015). The fibroblast growth factor signaling pathway. *Wiley Interdisciplinary Reviews: Developmental Biology*, *4*(3), 215–266. https://doi.org/10.1002/wdev.176

Park, M. J., Shen, H., Spaeth, J. M., Tolvanen, J. H., Failor, C., Knudtson, J. F., McLaughlin, J., Halder, S. K., Yang, Q., Bulun, S. E., Al-Hendy, A., Schenken, R. S., Aaltonen, L. A., & Boyer, T. G. (2018). Oncogenic exon 2 mutations in Mediator subunit MED12 disrupt allosteric activation of cyclin C-CDK8/19. *The Journal of Biological Chemistry*, *293*(13), 4870–4882. https://doi.org/10.1074/JBC.RA118.001725

Radzisheuskaya, A., Le Bin Chia, G., Dos Santos, R. L., Theunissen, T. W., Castro, L. F. C., Nichols, J., & Silva, J. C. R. (2013). A defined Oct4 level governs cell state transitions of pluripotency entry and differentiation into all embryonic lineages. *Nature Cell Biology*, *15*(6), 579–590. https://doi.org/10.1038/ncb2742

Raina, D., Bahadori, A., Stanoev, A., Protzek, M., Koseska, A., & Schröter, C. (2021). Cell-cell communication through FGF4 generates and maintains robust proportions of differentiated cell types in embryonic stem cells. *Development*, *148*(21), 1–31. https://doi.org/10.1242/DEV.199926

Ran, F. A., Hsu, P. D., Wright, J., Agarwala, V., Scott, D. A., & Zhang, F. (2013). Genome engineering using the CRISPR-Cas9 system. *Nature Protocols*, *8*(11), 2281–2308. https://doi.org/10.1038/NPROT.2013.143

Robin, X., Turck, N., Hainard, A., Tiberti, N., Lisacek, F., Sanchez, J. C., & Müller, M. (2011). pROC: An open-source package for R and S+ to analyze and compare ROC curves. *BMC Bioinformatics*, *12*(1), 1–8. https://doi.org/https://doi.org/10.1186/1471-2105-12-77

Rocha, P. P., Scholze, M., Bleiß, W., & Schrewe, H. (2010). Med12 is essential for early mouse development and for canonical Wnt and Wnt/PCP signaling. *Development*, *137*(16), 2723–2731. https://doi.org/10.1242/dev.053660

Rosales-Alvarez, R. E., Rettkowski, J., Herman, J. S., Dumbović, G., Cabezas-Wallscheid, N., & Grün, D. (2023). VarID2 quantifies gene expression noise dynamics and unveils functional heterogeneity of ageing hematopoietic stem cells. *Genome Biology*, *24*(1). https://doi.org/10.1186/s13059-023-02974-1

Schindelin, J., Arganda-carreras, I., Frise, E., Kaynig, V., Pietzsch, T., Preibisch, S., Rueden, C., Saalfeld, S., Schmid, B., Tinevez, J., White, D. J., Hartenstein, V., Tomancak, P., & Cardona, A. (2012). Fiji - an Open Source platform for biological image analysis. *Nature Methods*, *9*(7), 676–682. https://doi.org/10.1038/nmeth.2019

Schmidt, U., Weigert, M., Broaddus, C., & Myers, G. (2018). Cell detection with star-convex polygons. *Lecture Notes in Computer Science*, *11071 LNCS*, 265–273. https://doi.org/10.1007/978-3-030-00934-2_30

Schröter, C., Rué, P., Mackenzie, J. P., & Arias, A. M. (2015). FGF/MAPK signaling sets the switching threshold of a bistable circuit controlling cell fate decisions in embryonic stem cells. *Development*, *142*(24), 4205–4216. https://doi.org/10.1242/DEV.127530/-/DC1

Schumacher, S., Fernkorn, M., Marten, M., Chen, R., Kim, Y. S., Bedzhov, I., & Schröter, C. (2024). Tissue-intrinsic beta-catenin signals antagonize Nodal-driven anterior visceral endoderm differentiation. *Nature Communications*, *15*(1). https://doi.org/10.1038/s41467-024-49380-0

Smith, A. (2017). Formative pluripotency: The executive phase in a developmental continuum. *Development*, *144*(3), 365–373. https://doi.org/10.1242/dev.142679

Soutourina, J. (2018). Transcription regulation by the Mediator complex. *Nature Reviews Molecular Cell Biology*, *19*(4), 262–274. https://doi.org/10.1038/nrm.2017.115

Stevens, J. L., Cantin, G. T., Wang, G., Shevchenko, A., Shevchenko, A., & Berk, A. J. (2002). Transcription control by E1A and MAP kinase pathway via Sur2 mediator subunit. *Science*, *296*(5568), 755–758. https://doi.org/10.1126/SCIENCE.1068943

Szklarczyk, D., Franceschini, A., Wyder, S., Forslund, K., Heller, D., Huerta-Cepas, J., Simonovic, M., Roth, A., Santos, A., Tsafou, K. P., Kuhn, M., Bork, P., Jensen, L. J., & Von Mering, C. (2015). STRING v10: protein-protein interaction networks, integrated over the tree of life. *Nucleic Acids Research*, *43*(Database issue), D447–D452. https://doi.org/10.1093/NAR/GKU1003

Tang, M., Kaymaz, Y., Logeman, B. L., Eichhorn, S., Liang, Z. S., Dulac, C., & Sackton, T. B. (2021). Evaluating single-cell cluster stability using the Jaccard similarity index. *Bioinformatics*, *37*(15), 2212–2214. https://doi.org/10.1093/BIOINFORMATICS/BTAA956

Tee, W. W., Shen, S. S., Oksuz, O., Narendra, V., & Reinberg, D. (2014). Erk1/2 activity promotes chromatin features and RNAPII phosphorylation at developmental promoters in mouse ESCs. *Cell*, *156*(4), 678–690. https://doi.org/10.1016/j.cell.2014.01.009

Tutter, A. V., Kowalski, M. P., Baltus, G. A., Iourgenko, V., Labow, M., Li., E., & Kadam, S. (2009). Role for Med12 in regulation of Nanog and Nanog target genes. *Journal of Biological Chemistry*, *284*(6), 3709–3718. https://doi.org/10.1074/jbc.M805677200

Villegas, F., Lehalle, D., Mayer, D., Rittirsch, M., Stadler, M. B., Zinner, M., Olivieri, D., Vabres, P., Duplomb-Jego, L., De Bont, E. S. J. M., Duffourd, Y., Duijkers, F., Avila, M., Geneviève, D., Houcinat, N., Jouan, T., Kuentz, P., Lichtenbelt, K. D., Thauvin-Robinet, C., … Betschinger, J. (2019). Lysosomal Signaling Licenses Embryonic Stem Cell Differentiation via Inactivation of Tfe3. *Cell Stem Cell*, *24*(2), 257–270. https://doi.org/10.1016/J.STEM.2018.11.021

Wamaitha, S. E., del Valle, I., Cho, L. T. Y., Wei, Y., Fogarty, N. M. E., Blakeley, P., Sherwood, R. I., Ji, H., & Niakan, K. K. (2015). Gata6 potently initiates reprograming of pluripotent and differentiated cells to extraembryonic endoderm stem cells. *Genes & Development*, *29*(12), 1239–1255. https://doi.org/10.1101/GAD.257071.114

Ying, Q. L., Wray, J., Nichols, J., Batlle-Morera, L., Doble, B., Woodgett, J., Cohen, P., & Smith, A. (2008). The ground state of embryonic stem cell self-renewal. *Nature*, *453*(7194), 519–523. https://doi.org/10.1038/nature06968

Youden, W. J. (1950). INDEX FOR RATING DIAGNOSTIC TESTS. *Cancer*, *3*(1), 32–35. https://doi.org/10.1002/1097-0142(1950)3:1<32::AID-CNCR2820030106>3.0.CO;2-3

Supplementary Figures

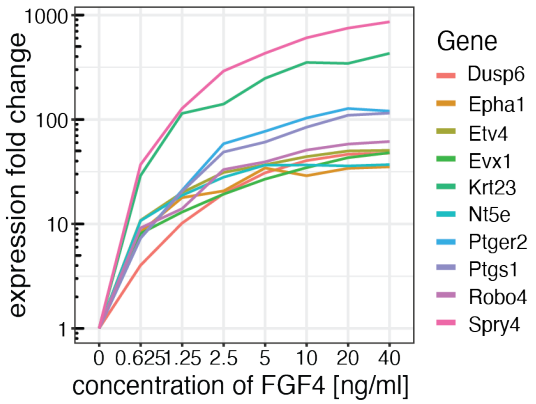

Fig. 1 Supp 1: *Spry4* is strongly upregulated upon FGF stimulation.

Expression fold change of the ten most upregulated genes upon FGF4 titration in *Fgf4* mutants. *Fgf4*-mutant *Spry4*$^{H2B\text{-}Venus/+}$ cells were transitioned from 2i + LIF medium containing 10% FBS to N2B27 supplemented with Chiron and LIF for 18 h, followed by 6 h of stimulation with indicated concentrations of FGF4 in N2B27 with Chiron.

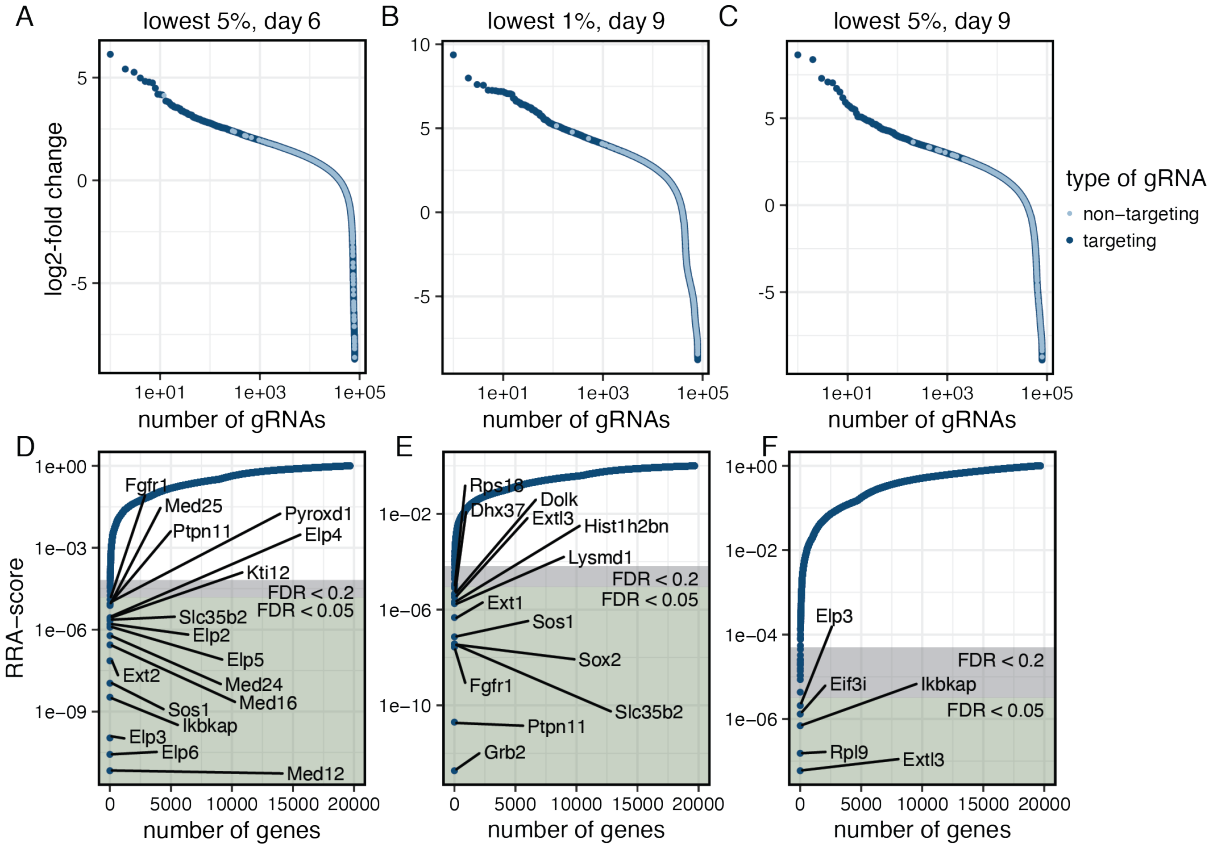

Fig. 1 Supp 2: Genome-wide CRISPR knockout screen results in robust enrichment of gRNAs and corresponding genes.

A - C Log 2-fold enrichment of gene-targeting (dark blue) and control gRNAs (light blue) in cells sorted for the lowermost 5% of H2B-Venus signal on day 6 after gRNA transduction (A), sorted for the

lowermost 1% on day 9 after transduction (B), or sorted for the the lowermost 5% on day 9 after transduction (C). **D** - **F** RRA scores for genes corresponding to enriched gRNAs identified in A - C.

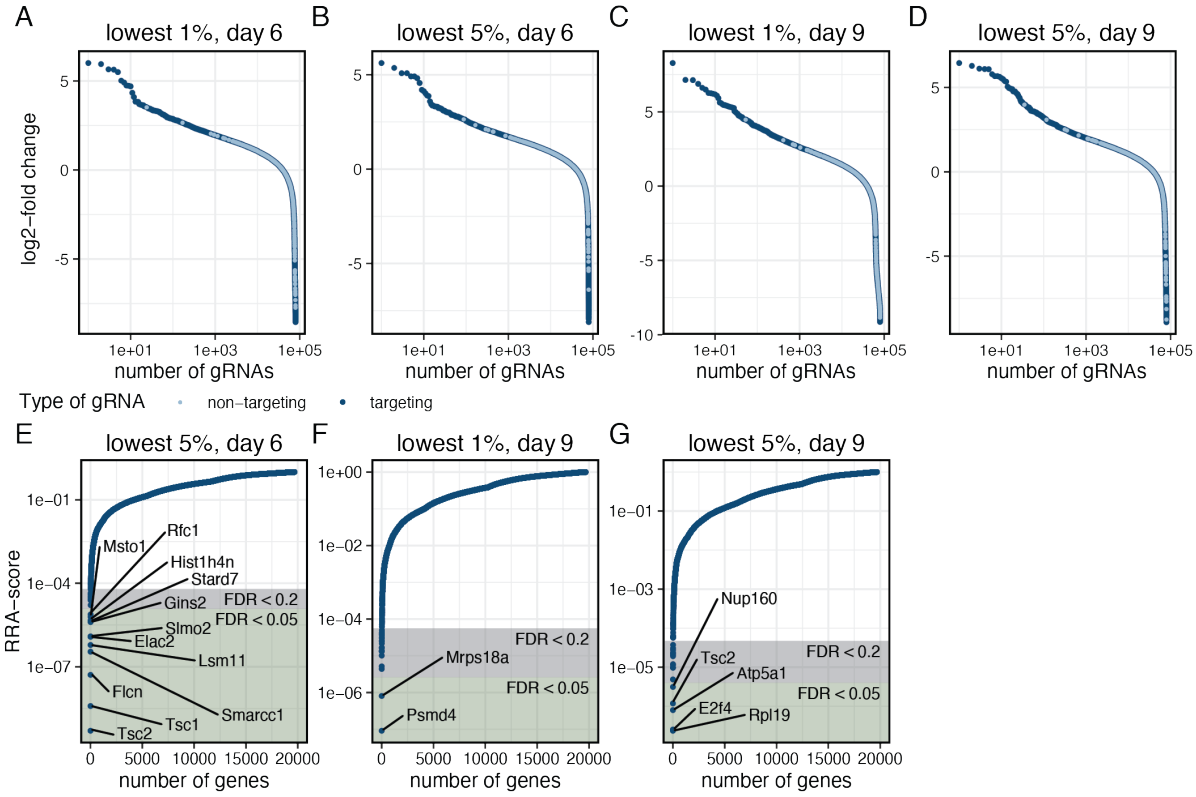

Fig. 2 Supp 1: Robust enrichment of gRNAs and corresponding genes that negatively regulate Spry4:H2B-Venus expression.

A - **D** Log 2-fold enrichment of gene-targeting (dark blue) and control gRNAs (light blue) in cells sorted for high H2B-Venus expression on different days as indicated.

E - **G** RRA scores for genes corresponding to enriched gRNAs identified in B - D. RRA scores for genes corresponding to gRNAs enriched in the 1% of the cells with highest fluorescence after 6 days are shown in Fig. 2A.

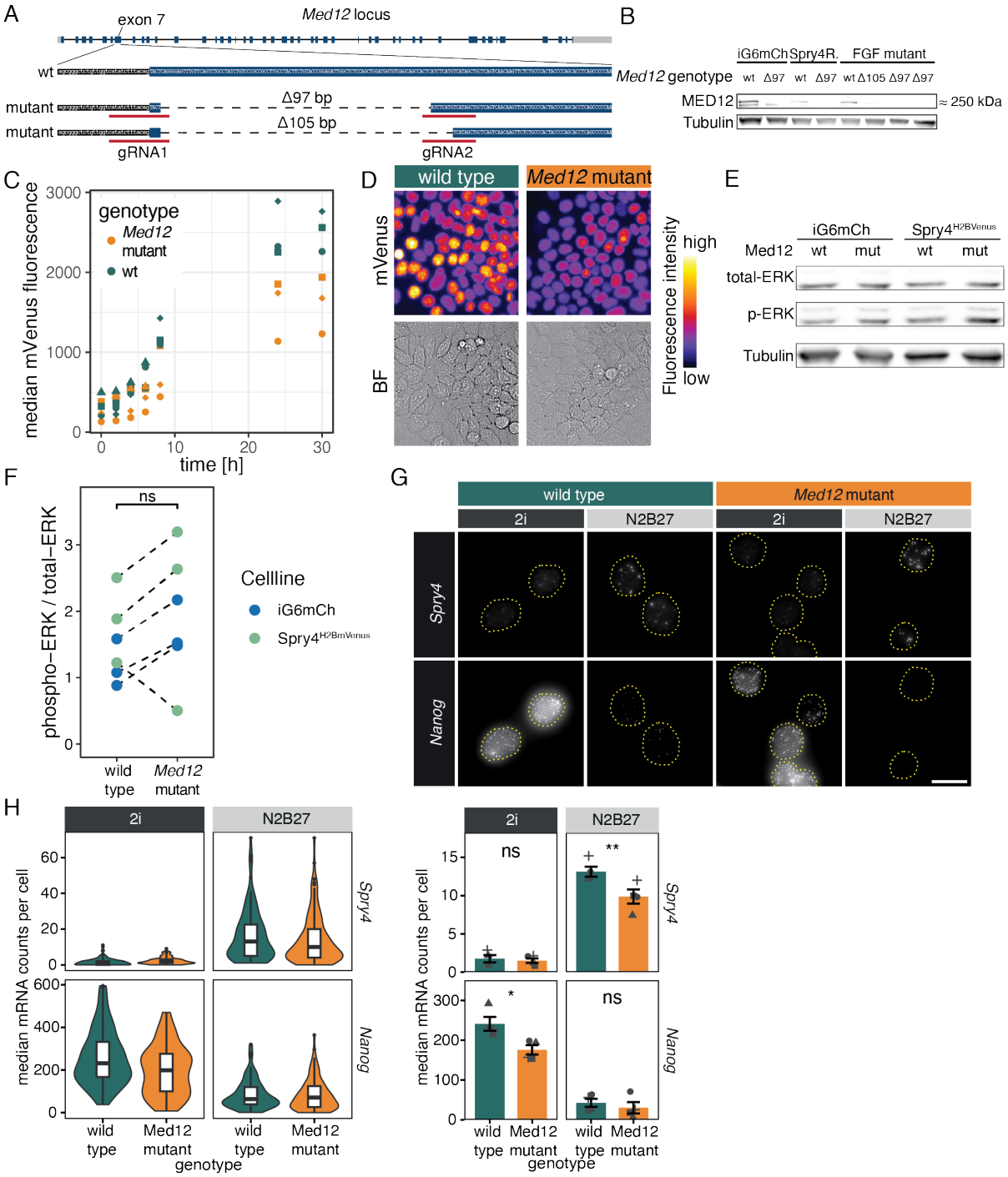

Fig. 3 Supp1: Generation of *Med12* mutant cell lines.

A Schematic of the *Med12* gene locus and the gRNAs used to create a *Med12* loss-of-function by deleting 97 or 105 bp of exon7. Intronic sequence in lowercase and black underline, exonic sequence in uppercase and blue underline.

B Immunoblotting for MED12 and Tubulin in cell lysates from independent monoclonal *Med12* mutant lines generated in different genetic genetic backgrounds. Δ97 and Δ105 indicate the type of exon7 deletion in each clone.

C *Spry4*$^{H2B\text{-}Venus/+}$ expression upon release from 2i + LIF to N2B27 in wild-type and *Med12*-mutant cells measured by flow cytometry. Data points show median fluorescence in each experiment. N = 3.

1109 **D** H2B-Venus expression in live wild-type and *Med12*-mutant *Spry4*$^{H2B\text{-}Venus/+}$ cells after 24 h of growth
1110 in N2B27 following release from 2i + LIF.
1111 **E** Immunoblotting of cell lysates from *Med12* wild type and *Med12*-mutant *Spry4*$^{H2B\text{-}Venus/+}$ and iGata6
1112 mESCs, stained for Tubulin, total- and phopsho-ERK.
1113 **F** Quantification of phospho-ERK signals from immunoblots, normalized to total-ERK. N=3. ns indicates
1114 $p \geq 0.05$, paired two-sided t-test.
1115 **G** Fluorescent in-situ hybridization staining of wild-type (left) and *Med12*-mutant cells (right) for *Spry4*
1116 (top) and *Nanog* (bottom) mRNAs in 2i medium, or 24h after transfer into N2B27.
1117 **H** Violin plots (left) and summary statistics of *Spry4* (top) and *Nanog* (bottom) mRNA numbers in wild-
1118 type and *Med12* mutant cells determined by in-situ hybridization as described in **G.** Violin Plots show
1119 one out of N = 4 replicates, n > 100 cells per replicate and condition.
1120

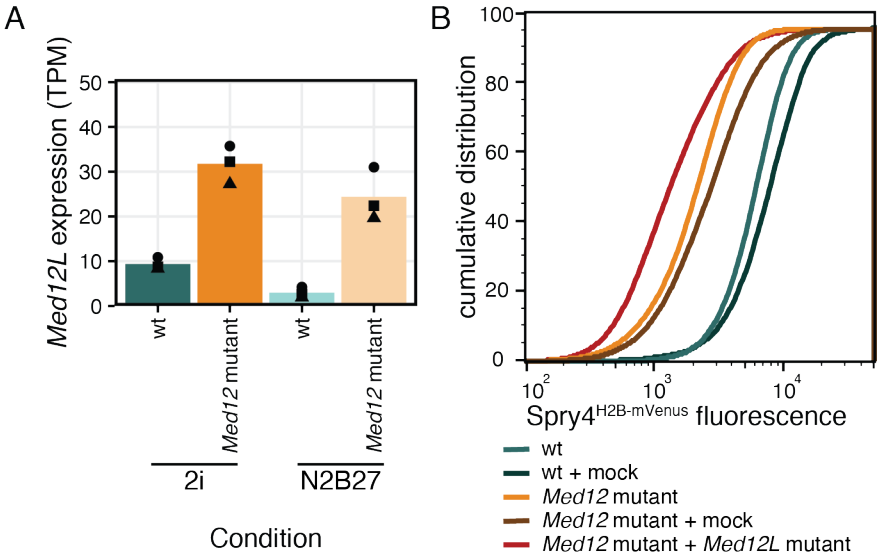

1121
1122 **Fig. 3 Supp 2: *Med12l* is upregulated upon loss of *Med12*.**
1123 **A** Expression of *Med12l* in wild-type and *Med12*-mutant cells (data from RNA-seq experiment in Fig.
1124 3A).
1125 **B** H2B-Venus expression in untransfected wild-type and *Med12*-mutant cells, and after transfection with
1126 mock or *Med12l*-targeting gRNAs. Expression was measured by flow cytometry 7 d after transfection
1127 and culture in ES + LIF medium.
1128

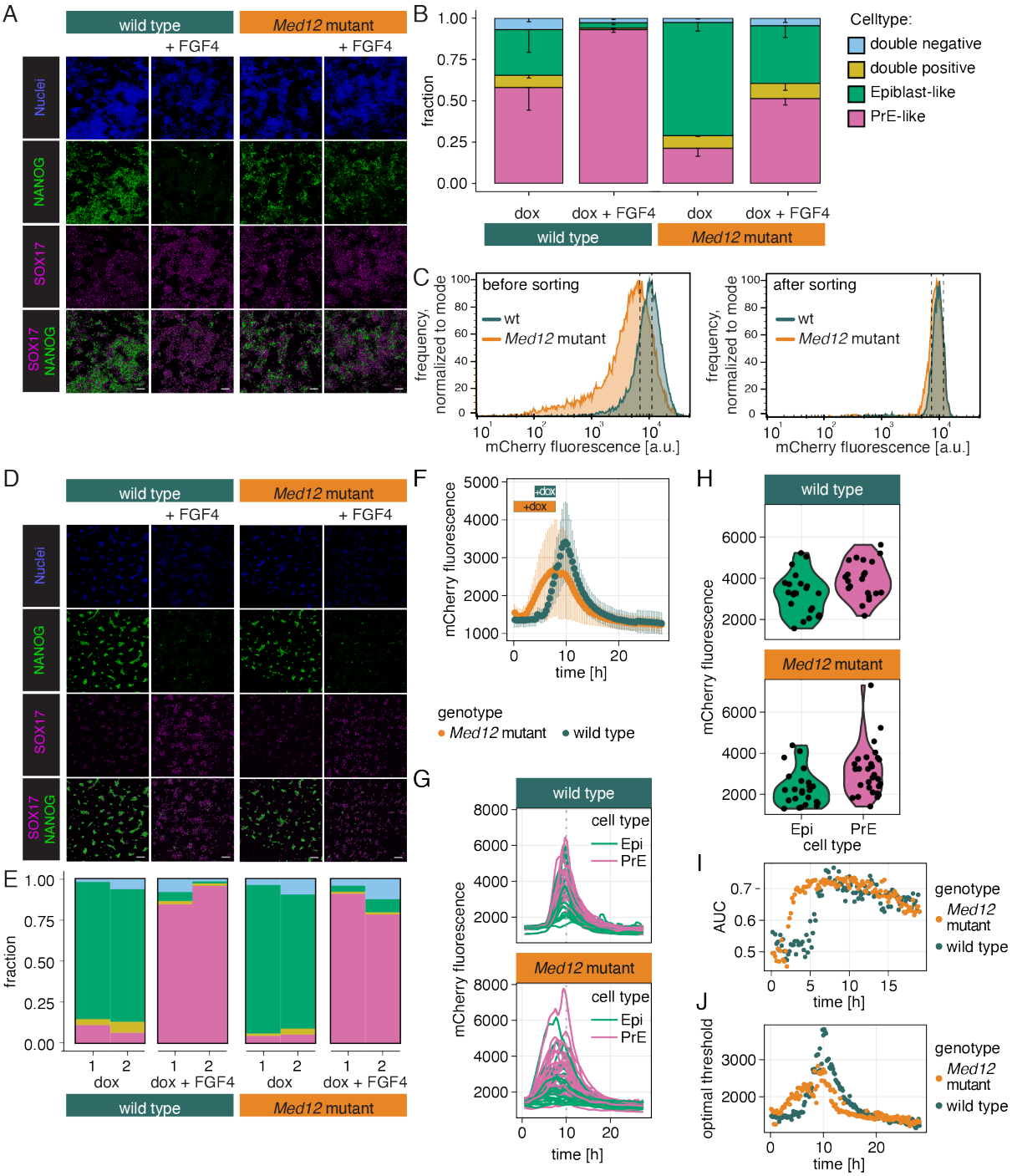

Fig. 4 Supp 1: PrE differentiation in *Med12* mutant cells.

A Immunostaining of the Epi-marker NANOG (green) and the PrE marker SOX17 (magenta) after 8 h of GATA6 induction and 20 h of differentiation with and without exogenous FGF4 in wild-type and *Med12*-mutant cells. Scale bar: 100 µm.

B Cell type proportions in wild-type and *Med12*-mutant cells differentiated as in (A). N=3, n > 1100 cells per replicate, error bars indicate SEM.

C Gata6-mCherry fluorescence after 8 h of dox induction measured by flow cytometry. Left shows distribution of expression levels in the whole population, right shows expression levels after flow sorting of cells with similar fluorescence intensity. Dashed lines indicate sorting gate.

1139 **D** Immunostaining of the Epi-marker NANOG (green) and the PrE marker SOX17 (magenta) after 8 h
1140 of GATA6 induction, flow sorting as described in (C), reseeding and 20 h of differentiation with and
1141 without exogenous FGF4 in wild-type and *Med12*-mutant cells. Scale bar: 100 µm.
1142 **E** Cell type proportions in wild-type and *Med12*-mutant cells differentiated as in (D). N=2, n > 500 cells
1143 per replicate.
1144 **F** Quantification of Gata6-mCherry expression dynamics from time-lapse movies during induction and
1145 differentiation. Boxes indicate induction times (8 h for *Med12* mutant, 4 h for wild type). Error bars
1146 indicate SD. One out of N = 5 replicates shown, n > 300 cells per time point.
1147 **G** Same experiment as in (E), but showing Gata6-mCherry fluorescence in single cells. Trace color
1148 indicates differentiation outcome determined by immunostaining (Epi: green; PrE: magenta).
1149 **H** Gata6-mCherry fluorescence in single cells 2 h after the end of induction, plotted separately for
1150 prospective Epi and PrE cells.
1151 **I** Predictive power of GATA6-mCherry expression determined as Area Under the Curve (AUC) from
1152 ROC-analysis.
1153 **J** Optimal GATA6-mCherry threshold to predict differentiation outcome determined by Youden's J
1154 statistic of ROC-analysis.
1155 **F - I** Data from one representative experiment out of N = 3 replicates, n ≥ 45 cells per genotype.
1156
1157

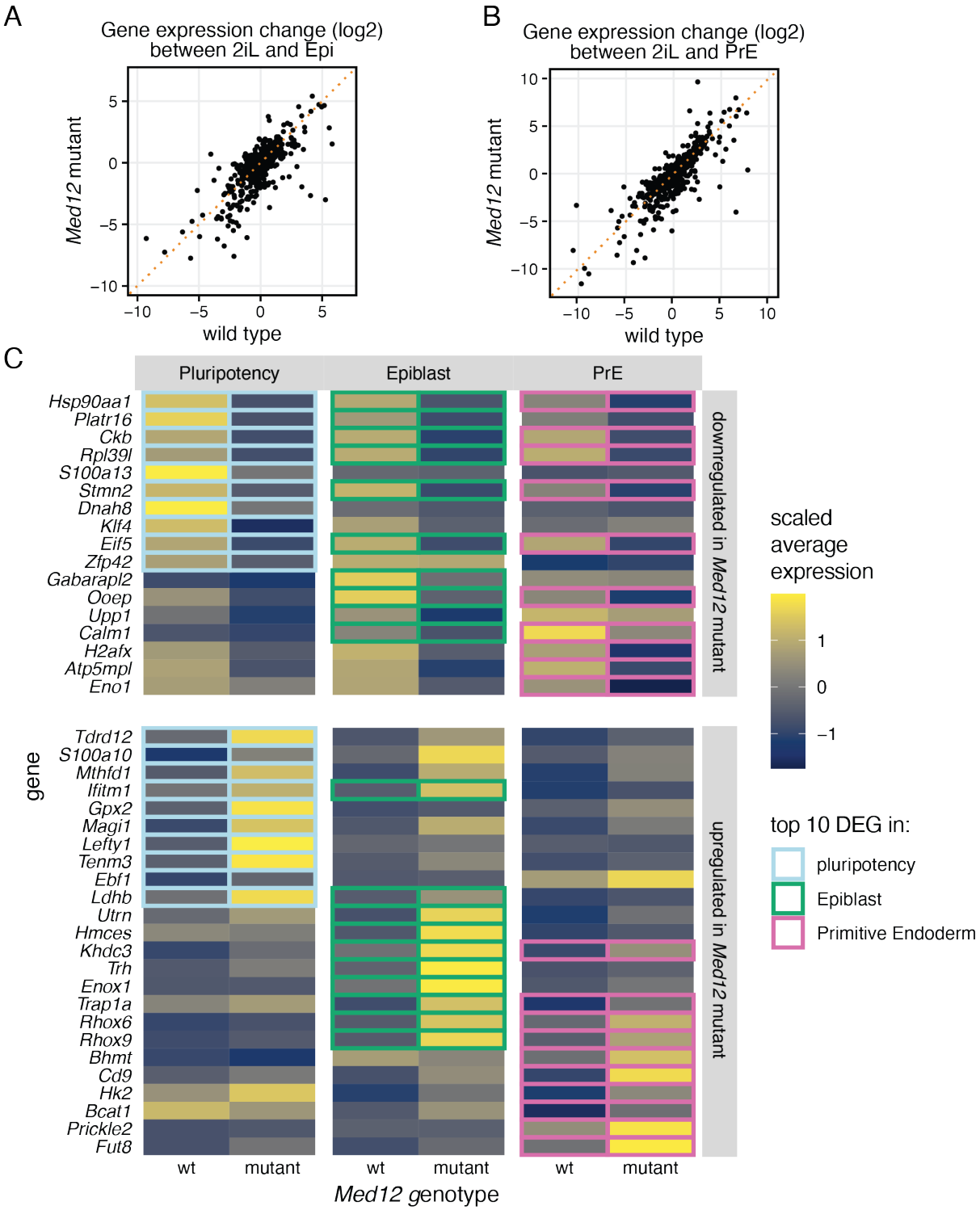

Fig. 4 Supp 2:

A and **B** Expression change of each gene upon differentiation from pluripotency (2iL) to Epi (A) and PrE (B) in wild-type versus *Med12*-mutant cells. Dotted, orange line indicates the unity line.

C Differentially expressed genes between *Med12* wild type and mutant cells for the three different cell states. Tile color shows scaled average gene expression, colored boxes indicate the 10 genes with the largest fold-change between *Med12* wild type and mutant cells in each cell state.

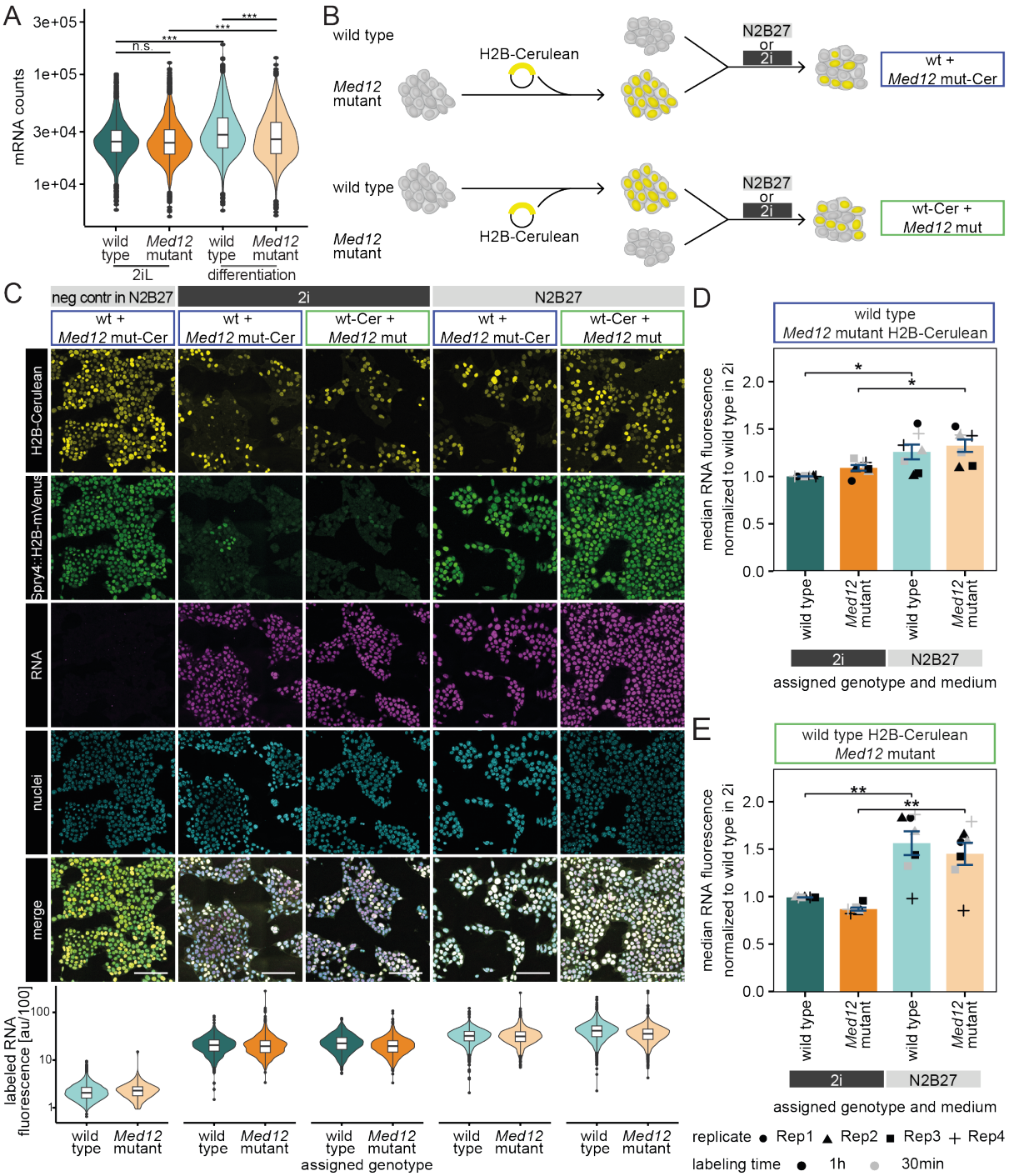

Fig. 4 Supp 3: Global RNA levels increase during differentiation of mESCs.

A Raw number of UMIs per cell detected by scRNAseq in wild-type and *Med12*-mutant cells. ns indicates $p \geq 0.05$, *** indicates $p \leq 0.001$, Bonferroni-adjusted Kolmogorov-Smirnov test.

B Schematic of H2B-labeling of *Med12* mutant (top) or wild type cells (bottom) to compate RNA production in pluripotency (2i) and differentiation (N2B27) conditions.

C Fluorescent images (upper panel) and violin plot of intensity (lower panel) of RNA-labeling with EU in 2i (dark grey) and N2B27 (light grey). Mixtures of genotypes were images in the same well, with one of them labeled with H2B-Cerulean (yellow) expression. For nuclei segmentation hoechst staining (cyan) was used and Spry4-H2B-mVenus-expression (green) confirmed differentiation in N2B27.

1175 **D, E** Quantification of intensity of RNA labeling based on cells assigned genotype based on their H2B-
1176 Cerulean expression (B). In (C) the *Med12*-mutant cell line was labeled with H2B-Cerulean, in (D) the
1177 wild-type line. N = 3, n > 750 cells. n.s. indicates p ≥ 0.05, * indicates p < 0.05 and ** indicates p < 0.01,
1178 paired two-sided t-test with Bonferroni multiple testing correction.
1179

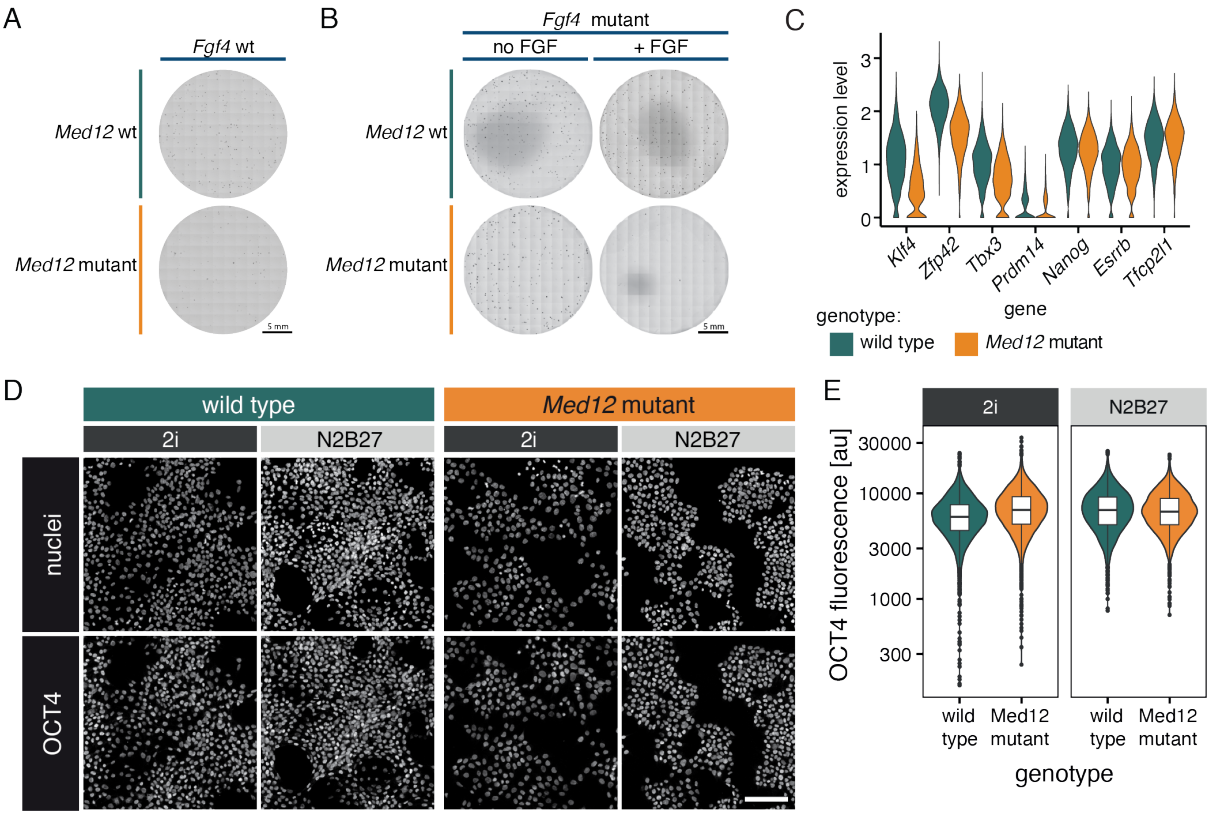

1180

1181 **Fig. 5 Supp 1: Reduced clonogenicity in *Med12* mutants compared to wild type.**
1182 **A** and **B** Representative images of plates from the clonogenicity assay depicted in Fig. 5A,
1183 corresponding to quantifications shown in Fig. 5B. **A** shows plates with wild-type and *Med12*-mutant
1184 cells in an *Fgf4* wild type background, **B** shows plates with wild-type and *Med12*-mutant cells in an *Fgf4*-
1185 mutant background without (left) and with (right) FGF4 supplementation.
1186 **C** Ln-transformed expression levels of same naïve pluripotency marker genes as in Fig. 5C,D from
1187 pluripotent cells of single cell sequencing experiment from Fig 4.
1188 **D** Immunostaining for OCT4 (Pou5f1) in wild-type and *Med12*-mutant cells in 2i and N2B27. Scale bar
1189 100 µm.
1190 **E** Quantification of OCT4 fluorescence per nucleus from cells stained as in (D).

Supplementary Table legends

Supp Table 1: Raw and processed data from CRISPR screen including detected counts of gRNAs and enriched genes.

Supp Table 2: Differentially expressed genes comparing wild-type and *Med12*-mutant cells in 2i and after 24 h differentiation in N2B27.

Supp Table 3: Differentially expressed genes in *Fgf4*-mutant and *Fgf4 Med12* double mutant cells upon FGF4 stimulation in N2B27.

Supp Table 4: Differentially expressed genes between the Epi- (cluster 1) and PrE-cells (cluster 0) determined by single cell RNA sequencing experiment.

Supp Table 5: Differentially expressed genes between wild-type and *Med12*-mutant cells separately in pluripotency conditions, the Epi- and PrE-cluster.

Supp Table 6: Raw and normalized counts of colonies detected in the colony formation assay.

Supp Table 7: Oligos used as gRNAs or PCR primers.

Supplementary Movie legends

Supp Movie 1: Timelapse imaging of H2B-Cerulean (blue) and iGata6-mCherry expression (red) in wild-type and Med12-mutant cells during Epi and PrE differentiation under same conditions as in Figure 3E. Following time lapse imaging, cells were immunostained for the Epi-marker NANOG (green) and the PrE marker SOX17 (magenta). Nuclei in immunostainings labelled with Hoechst dye (cyan). Scale bar: 50 µm.